Spectral-element simulations of global seismic wave propagation—I. Validation

Dimitri Komatitsch and Jeroen Tromp

Seismological Laboratory, California Institute of Technology, Pasadena, California 91125, *USA. E-mail: jtromp@gps.caltech.edu*

SUMMARY

We use a spectral-element method to simulate seismic wave propagation throughout the entire globe. The method is based upon a weak formulation of the equations of motion and combines the flexibility of a finite-element method with the accuracy of a global pseudospectral method. The finite-element mesh honours all first- and second-order discontinuities in the earth model. To maintain a relatively constant resolution throughout the model in terms of the number of grid points per wavelength, the size of the elements is increased with depth in a conforming fashion, thus retaining a diagonal mass matrix. In the Earth's mantle and inner core we solve the wave equation in terms of displacement, whereas in the liquid outer core we use a formulation based upon a scalar potential. The three domains are matched at the inner core and core–mantle boundaries, honouring the continuity of traction and the normal component of velocity. The effects of attenuation and anisotropy are fully incorporated. The method is implemented on a parallel computer using a message passing technique. We benchmark spectral-element synthetic seismograms against normal-mode synthetics for a spherically symmetric reference model. The two methods are in excellent agreement for all body- and surface-wave arrivals with periods greater than about 20 s.

Key words: body waves, elastodynamics, global seismology, numerical techniques, seismic wave propagation, surface waves.

1 INTRODUCTION

The calculation of accurate synthetic seismograms for fully 3-D global earth models poses a formidable challenge. The effects of an anisotropic asthenosphere, a slow crust with highly variable thickness, sharp fluid–solid discontinuities at the inner core (ICB) and core–mantle (CMB) boundaries, ellipticity, free-surface topography and attenuation must all be accounted for. In this article we demonstrate that the spectral-element method (SEM), introduced more than 15 years ago in computational fluid mechanics (Patera 1984; Maday & Patera 1989; Fischer & Rønquist 1994), can meet this challenge. The method has been used to accurately model wave propagation on local and regional scales, both in 2-D (Priolo *et al.* 1994; Komatitsch 1997; Faccioli *et al.* 1997; Komatitsch & Vilotte 1998) and in 3-D (Komatitsch 1997; Faccioli *et al.* 1997; Komatitsch & Vilotte 1998; Seriani 1998; Komatitsch & Tromp 1999; Paolucci *et al.* 1999). Previous publications have documented that the more specific aspects of global wave propagation can be dealt with by the SEM: Komatitsch & Vilotte (1998), Komatitsch & Tromp (1999) and Paolucci *et al.* (1999) demonstrate that the effects of free surface topography can be accommodated; Komatitsch *et al.* (2000a) show that fluid–solid boundaries can be accurately modelled; Seriani *et al.* (1995) and Komatitsch *et al.* (2000b) incorporate effects due to anisotropy, and Komatitsch & Tromp (1999) implement attenu-

ation. In this article we combine all these ingredients to tackle the problem of global wave propagation.

For spherically symmetric earth models, normal-mode summation is the preferred method for the calculation of synthetic seismograms (e.g. Dahlen & Tromp 1998). Normal-mode synthetics are accurate typically for periods greater than about 8 s (i.e. just above the microseismic noise band) and involve the summation of a few hundred thousand modes. The effects of fluid–solid boundaries, transverse isotropy with a radial symmetry axis and radial models of attenuation can all be accommodated. In this article we benchmark our SEM synthetic seismograms against reference normal-mode synthetics calculated for the Preliminary Reference Earth Model (PREM) (Dziewonski & Anderson 1981).

The SEM has been previously applied to the problem of 3-D global wave propagation in innovative work by Chaljub (2000), Chaljub *et al.* (2001) and Capdeville *et al.* (2002). They use a so-called 'mortar' version of the SEM (Bernardi *et al.* 1990, 1994; Lahaye *et al.* 1997), which allows for non-conforming meshes in which each side of every element does not have to match up exactly with the side of a neighbouring element. This makes mesh design more flexible, as it allows one to use smaller elements in the upper part of the model where wave speeds are slowest. There is, however, a significant increase in the complexity and cost of the implementation because the mass matrix is no longer diagonal on

the non-conforming interfaces. As a result, an iterative solver has to be used to solve the non-diagonal system. Here we use a classical SEM based upon a conforming mesh that retains a diagonal mass matrix. Chaljub (2000) and Capdeville *et al.* (2002) incorporate the effects of self-gravitation in a subsequent article (Komatitsch & Tromp 2002), but they do not incorporate anisotropy or attenuation or the crust at short periods. Capdeville *et al.* (2002) deal with problems posed by the fluid outer core by introducing an efficient coupling technique, which matches a normal-mode solution in the core to a SEM in the mantle. This allows one to reduce the cost of the method by assuming a spherically symmetric solution in the core and using spectral elements only in the upper part of the model. However, the requirement that the matching surface be strictly spherically symmetric precludes the incorporation of effects due to CMB topography or the Earth's ellipticity. Tromp & Komatitsch (2000) used a SEM to simulate wave propagation in a portion of the globe. In this article we extend the simulations to the entire globe and incorporate effects due to anisotropy, attenuation and the solid inner core. We implement the fluid–solid matching conditions using a simple and efficient domain decomposition technique.

Other researchers have attempted to simulate 3-D global wave propagation based upon a coupled-mode approach, in which the modes of a 3-D earth model are expressed as a sum over the modes of a spherically symmetric earth model (e.g. Park 1986; Park & Yu 1992; Lognonné & Romanowicz 1990; Capdeville *et al.* 2000), or direct-solution methods, which use more general basis functions (e.g. Hara *et al.* 1991; Geller & Ohminato 1994; Takeuchi *et al.* 2000). Coupled-mode and direct-solution synthetics are expensive to calculate, particularly for models with strong lateral variations which require a wide coupling bandwidth. Effects due to boundary undulations are linearized, which makes it difficult to accommodate significant variations in crustal thickness. The finite-difference technique (e.g. Igel & Weber 1996; Chaljub & Tarantola 1997; Thomas *et al.* 2000) provides an alternative approach to the calculation of global synthetics. It is well-known, however, that finite-difference methods are inaccurate for surface waves because of numerical dispersion (e.g. Robertsson 1996). Furthermore, the design of a grid for the globe poses geometrical difficulties because of the decrease in grid spacing with depth. In addition, diffracted phases are hard to model accurately, in particular at the CMB, because of the staggered nature of the grid. Finally, pseudospectral methods have been used to address the problem (e.g. Tessmer *et al.* 1992; Carcione & Wang 1993; Furumura *et al.* 1998; Igel 1999). As in finite-difference methods, gridding the entire globe has not yet been accomplished because of difficulties related to the spherical geometry, and the accurate implementation of the free surface boundary condition is problematic. In addition, major velocity discontinuities in the model are difficult to take into account because of the global polynomial nature of the solution. In practice, coupled-mode, direct-solution, finite-difference and pseudospectral methods often have to assume that earth models are 2-D axisymmetric to reduce the computational burden. The COSY project (Igel & Geller 2000) brought together several research groups in an attempt to benchmark numerical algorithms for 1-D and 3-D Earth models. The results are summarized in a special issue of *Physics of the Earth and Planetary Interiors* (Volume 119, 2000) which illustrates many of the difficulties associated with the problem.

2 MESHING THE GLOBE

As in any finite-element method, a first crucial step towards the accurate simulation of 3-D seismic wave propagation is the design

of a mesh: the model volume Ω needs to be subdivided into a number of non-overlapping elements Ω_e, $e = 1, \ldots, n_e$, such that $\Omega = \cup_{e=1}^{n_e} \Omega_e$. In this section we highlight some of the basic ingredients of mesh design, which are classical finite-element results. For a detailed introduction to finite-element methods the reader is referred to Zienkiewicz (1977) and Hughes (1987).

A classical spectral-element method relies upon a mesh of hexahedral finite elements Ω_e that are isomorphous to the cube. Tetrahedra, which are classical in finite-element methods, are excluded in the SEM because of the tensorization of the polynomial basis that is required to obtain an exactly diagonal mass matrix, as will be explained in Section 3. The six sides of each hexahedral element must match up exactly with the sides of neighbouring elements. Such a mesh is traditionally called a conforming mesh in the finite-element literature. For reasons of accuracy, a good mesh should honour all the major first- and second-order discontinuities in the model, and the size of the elements should reflect the distribution of wave speeds, such that one maintains a relatively similar number of grid points per wavelength throughout the model. Since wave speed generally increases with depth, this implies that the elements should become gradually larger with depth. These requirements make the design of a mesh for the globe challenging.

The mapping between Cartesian points $\mathbf{x} = (x, y, z)$ within a deformed, hexahedral element Ω_e and the reference cube may be written in the form

$$\mathbf{x}(\boldsymbol{\xi}) = \sum_{a=1}^{n_a} N_a(\boldsymbol{\xi})\mathbf{x}_a. \tag{1}$$

Points within the reference cube are denoted by the vector $\boldsymbol{\xi} = (\xi, \eta, \zeta)$, where $-1 \le \xi \le 1$, $-1 \le \eta \le 1$ and $-1 \le \zeta \le 1$. The geometry of our finite elements is defined in terms of $n_a = 27$ control points, or anchors, $\mathbf{x}_a$, as shown in Fig. 1. The n_a shape functions N_a are triple products of degree 2 Lagrange polynomials. The three Lagrange polynomials of degree 2 with three control points $\xi_0 = -1$, $\xi_1 = 0$, and $\xi_2 = 1$ are $\ell_0^2(\xi) = \frac{1}{2}\xi(\xi - 1)$, $\ell_1^2(\xi) = 1 - \xi^2$ and $\ell_2^2(\xi) = \frac{1}{2}\xi(\xi + 1)$. Given the choice of anchors $\mathbf{x}_a$, the shape functions N_a determine the geometry of the element.

A small volume $dx\, dy\, dz$ within a given finite element is related to a volume $d\xi\, d\eta\, d\zeta$ in the reference cube by $dx\, dy\, dz = J d\xi\, d\eta\, d\zeta$, where the Jacobian J of the mapping is
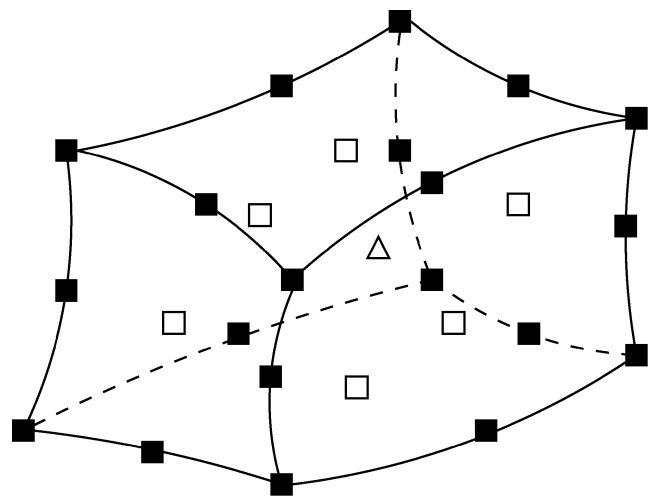

Figure 1. The geometry of each of the curved hexahedra is defined by 27 control nodes. This is a schematic example of a curved element and its anchors.

given by $J = |\partial(x, y, z)/\partial(\xi, \eta, \zeta)|$. The partial derivative matrix $\partial\mathbf{x}/\partial\boldsymbol{\xi}$ needed for the calculation of J is obtained by analytically differentiating the mapping (eq. 1). Partial derivatives of the shape functions N_a are defined in terms of Lagrange polynomials of degree 2 and their derivatives. One needs to ensure that the mapping (eq. 1) is unique and invertible, i.e. $\boldsymbol{\xi}(\mathbf{x})$ should be well-defined and the Jacobian J should never vanish. As in any finite-element method (e.g. Hughes 1987), the behaviour of the Jacobian J is controlled by the geometry of the mesh, and is a measure of its quality.

We will see that modelling interactions between the fluid and solid parts of the model at the CMB and ICB requires the evaluation of surface integrals. The mesh on a fluid–solid discontinuity Γ consists of boundary elements Γ_b, $b = 1, \ldots, n_b$, such that $\Gamma = \cup_{b=1}^{n_b} \Gamma_b$. The quadrilateral boundary elements Γ_b are simply the bottom or top sides of hexahedral volume elements Ω_e that border the CMB or ICB. They are isomorphous to the square. Let $-1 \le \xi \le 1, -1 \le \eta \le 1$ denote points in the square, and let $\mathbf{x}$ denote points in a boundary element Γ_b. The mapping between points in a quadrilateral boundary element and the reference square may be written in the form

$$\mathbf{x}(\xi, \eta) = \sum_{a=1}^{n_a} N_a(\xi, \eta)\mathbf{x}_a. \tag{2}$$

We use nine anchors $\mathbf{x}_a$ to describe the geometry of a boundary element Γ_b, which is the number of anchors that lie on one face of a hexahedral volume element Ω_e shown in Fig. 1. The nine shape functions $N_a(\xi, \eta)$ are double products of Lagrange polynomials of degree 2.

The orientation of the reference square is chosen such that the unit outward normal, $\hat{\mathbf{n}}$, to a boundary element, Γ_b, is given by

$$\hat{\mathbf{n}} = \frac{1}{J_b} \frac{\partial\mathbf{x}}{\partial\boldsymbol{\xi}} \times \frac{\partial\mathbf{x}}{\partial\boldsymbol{\eta}}, \tag{3}$$

where J_b denotes the Jacobian of the transformation,

$$J_b = \left\| \frac{\partial\mathbf{x}}{\partial\boldsymbol{\xi}} \times \frac{\partial\mathbf{x}}{\partial\boldsymbol{\eta}} \right\|. \tag{4}$$

To calculate the Jacobian, J_b, and the unit outward normal, $\hat{\mathbf{n}}$, one needs to determine the six partial derivatives $\partial\mathbf{x}/\partial\boldsymbol{\xi}$ and $\partial\mathbf{x}/\partial\boldsymbol{\eta}$. This is accomplished by analytically differentiating the mapping (eq. 2).

The mesh we use is based upon the concept of the 'quasi-uniform gnomonic projection', or 'cubed sphere' (Sadourny 1972; Ronchi *et al.* 1996; Taylor *et al.* 1997), which was introduced for global wave propagation problems by Taylor *et al.* (1997) and Chaljub (2000). The key idea is to map each of the six sides of the cube to the surface of the sphere. Labelling the six faces of the cube by Roman numerals I–VI, on each individual face we introduce Cartesian coordinates (α, β) such that $-\pi/4 \le \alpha \le \pi/4$ and $-\pi/4 \le \beta \le \pi/4$ map out the face, as shown in Fig. 2. Next, let the Cartesian coordinates (x, y, z) denote points on the surface of a sphere with radius r, such that $r = (x^2 + y^2 + z^2)^{1/2}$, and define the auxiliary variables $X = \tan\alpha$, $Y = \tan\beta$ and $Z = r(1 + X^2 + Y^2)^{-1/2}$. Then the mapping from each of the six faces of the cube to the surface of a sphere with radius r is defined by (e.g. Ronchi *et al.* 1996; Chaljub 2000):

Face I: $x = Z,$ $y = XZ,$ $z = YZ,$

Face II: $x = -Z,$ $y = -XZ,$ $z = YZ,$

Face III: $x = -XZ,$ $y = Z,$ $z = YZ,$
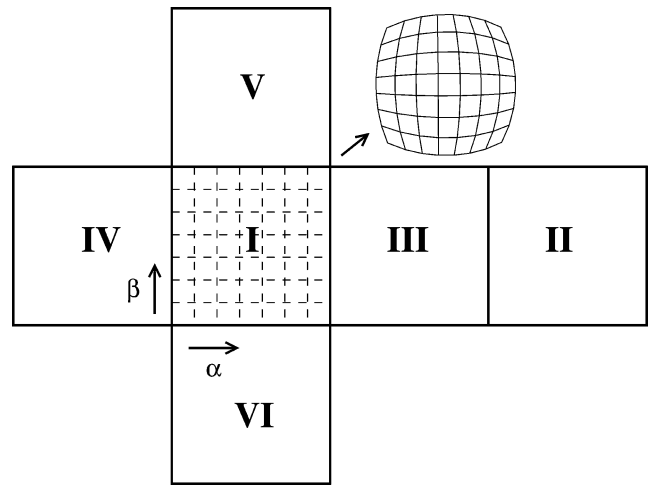
Face IV: $x = XZ,$ $y = -Z,$ $z = YZ,$

Figure 2. View of the six building blocks that constitute the cubed sphere. Each of the six faces I–VI of the cube is represented by an equidistant mesh in terms of surface coordinates $-\pi/4 \le \alpha \le \pi/4$ and $-\pi/4 \le \beta \le \pi/4$. Analytical relations map the six faces of the cube to the surface of the sphere, resulting in the angularly equidistant mesh shown to the top right for one of the six faces.

Face V: $x = -YZ,$ $y = XZ,$ $z = Z,$

Face VI: $x = YZ,$ $y = XZ,$ $z = -Z.$

In this fashion an equidistant grid in α and β on each face of the cube is mapped to an angularly equidistant grid on the surface of the sphere with radius r. As underlined by Ronchi *et al.* (1996), this gives a mesh on the surface of the sphere with smooth variations of the Jacobian, which is a requirement for good mesh design. By using the cubed-sphere mapping twice, once for the free surface of the model and a second time at the ICB, and using a linear interpolation in the radial direction between these two surface mappings, we obtain the mesh shown in Fig. 3. Note that the cubed sphere consists of six of these building blocks, or chunks, that have their origin in the six faces of the cube (Fig. 2).

Unfortunately, the mesh in Fig. 3 is not suitable for numerical simulations of 3-D wave propagation, because the elements naturally decrease in size with depth due to the spherical geometry. To
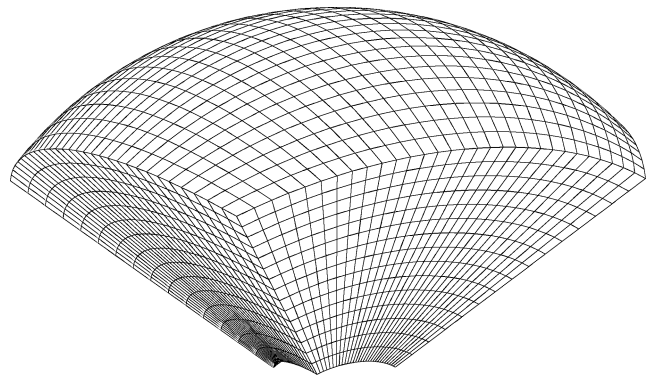

Figure 3. By using the cubed sphere mapping illustrated in Fig. 2 twice, first at the free surface and a second time at the ICB, and using a standard linear interpolation in the radial direction between these two surfaces, we obtain the mesh shown in the figure. This mesh has the undesirable property that the size of the elements decreases dramatically with depth. To maintain a relatively constant number of grid points per wavelength, element size should increase with depth.
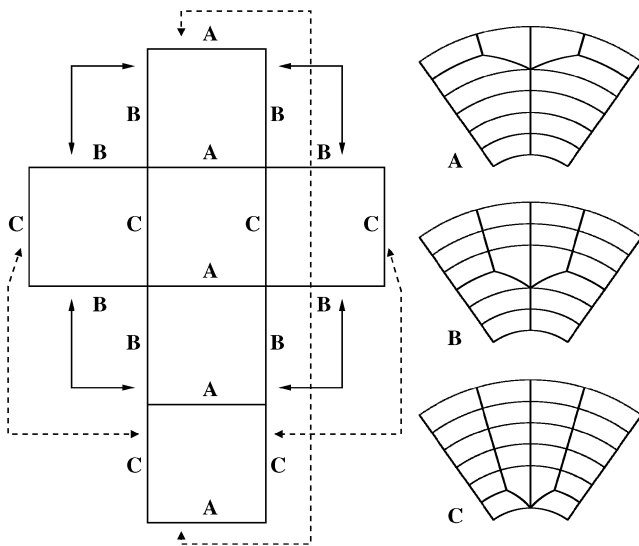
Figure 4. Mesh size needs to be increased in the globe as a function of depth to maintain a similar number of grid points per wavelength throughout the model. This is accomplished in three stages. Left: top view of the six building blocks that constitute the cubed sphere. Besides a top and bottom, each block has four sides that need to match up exactly with four other blocks to complete the cube, as indicated by the arrows. Schematically, these four sides have one of three designs: A, B or C, as illustrated on the right. When the six blocks are fitted together to make the entire globe, they match perfectly.

Figure 5. To avoid a mesh singularity associated with the Earth's centre, we place a cube at the centre of the solid inner core. We use a simple linear interpolation to create the mesh between the surface of the central cube and the cubed sphere mesh at the ICB. This figure shows the actual mesh used within the solid inner core. Note that there is a layer of three elements between the ICB and the central cube. Note also that element size within the central cube is not constant; this reflects a match-up with the angularly equidistant mesh at the ICB.

maintain a relatively similar number of grid points per wavelength the elements should instead increase in size, because seismic velocities in PREM generally increase with depth. An increase in element size can be obtained by first doubling the mesh in one lateral direction, and subsequently, at a greater depth, increasing its size in the other lateral dimension (e.g. Komatitsch & Tromp 1999). Increasing the mesh size with depth in a single chunk in this fashion is therefore straightforward. However, accomplishing this for more than one chunk in such a manner that each element on the side of one chunk matches up perfectly with an element on the side of a neighbouring chunk, in order to obtain a geometrically conforming mesh for the entire sphere, is more difficult. Fig. 4 illustrates schematically how this may be accomplished based upon a three-stage doubling as a function of depth. Note that there are three types of chunks: AB, AC, and BC. In each of the types the doubling is performed at different levels, such that the final six chunks fit together perfectly to make the entire globe based upon the cubed-sphere mapping. The main drawbacks of this mesh are the transition regions in which the doublings are implemented, because some resolution is lost due to the irregular shape of the elements. As mentioned earlier, an alternative is the use of a non-conforming mesh in the context of the 'mortar' method (Chaljub 2000), with the related complexity of implementation and the loss of a diagonal matrix system.

To avoid singularities at the Earth's centre, Chaljub (2000) introduced the idea of placing a cube around the centre of the inner core. The mesh within this cube needs to match up with the cubed sphere mesh at the ICB. The mapping between this spherical surface and the surface of the cube in the inner core is obtained by simple linear interpolation between the two surfaces. Fig. 5 shows the actual mesh used in the simulations for the inner core. Note that the mesh at the surface of the cube is not regular, but rather a flat version of the cubed sphere mapping shown in Fig. 3.
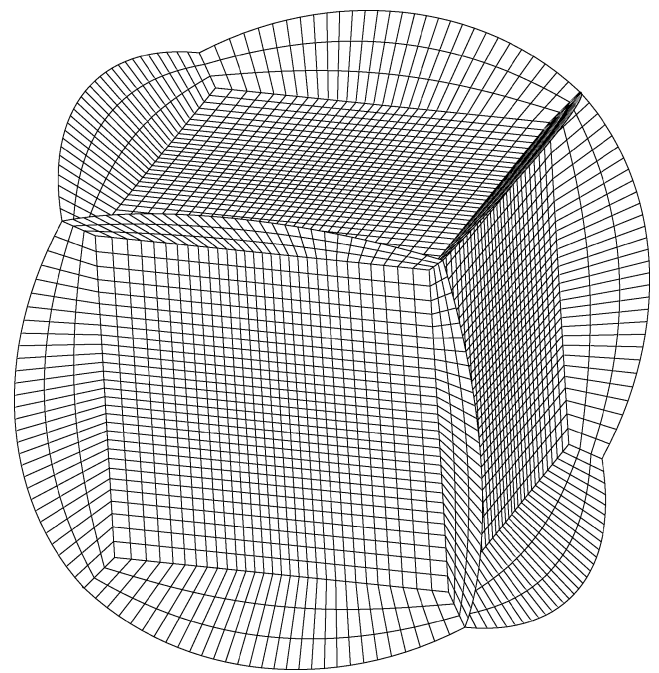
The mesh used in the 3-D simulations is shown in Fig. 6 and is designed to honour all first-order discontinuities in the Preliminary Reference Earth Model (PREM) (Dziewonski & Anderson 1981), which are the Moho at a depth of 24.4 km, the upper-mantle discontinuities at depths of 220 km, 400 km and 670 km, the CMB, and the ICB. It also honours second-order discontinuities at 600 km, 771 km and at the top of D''. The mesh is doubled in size once below the Moho, a second time below the 670 km discontinuity and a third time just above the ICB. Each of the six chunks has 240×240 elements at the free surface and, as a result of the three doublings, 30×30 elements at the ICB.

The radial density and velocity profiles of the model are determined by PREM. The 3 km thick water layer and the lower crust of PREM have been replaced by PREM upper crust, such that our model has a homogeneous crust with a thickness of 24.4 km and the constant properties of the PREM upper crust. The reason for this simplification is that the exact location of the boundary between the upper and lower crust can only be honoured by using at least two layers of finite elements in the crust, which would increase the computer memory requirements too dramatically. Of course the Earth's real crust is very different from that of PREM, which uses an average of the oceanic and continental crust. The depth of the associated upper/lower crust boundary therefore has little meaning at the global scale. PREM has a transversely isotropic asthenosphere between 24.4 km and 220 km, which is incorporated in our SEM simulations. We will consider wave propagation in PREM with and without incorporating attenuation. Normal-mode catalogues with a shortest period of 8 s were calculated for identical versions of PREM to obtain elastic and anelastic reference solutions.
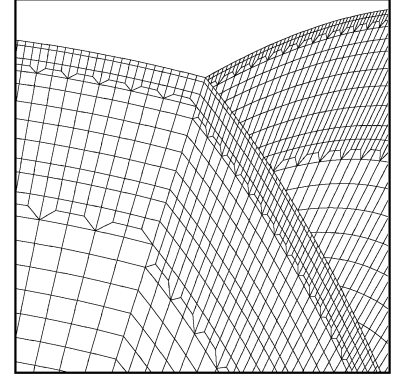
(a)
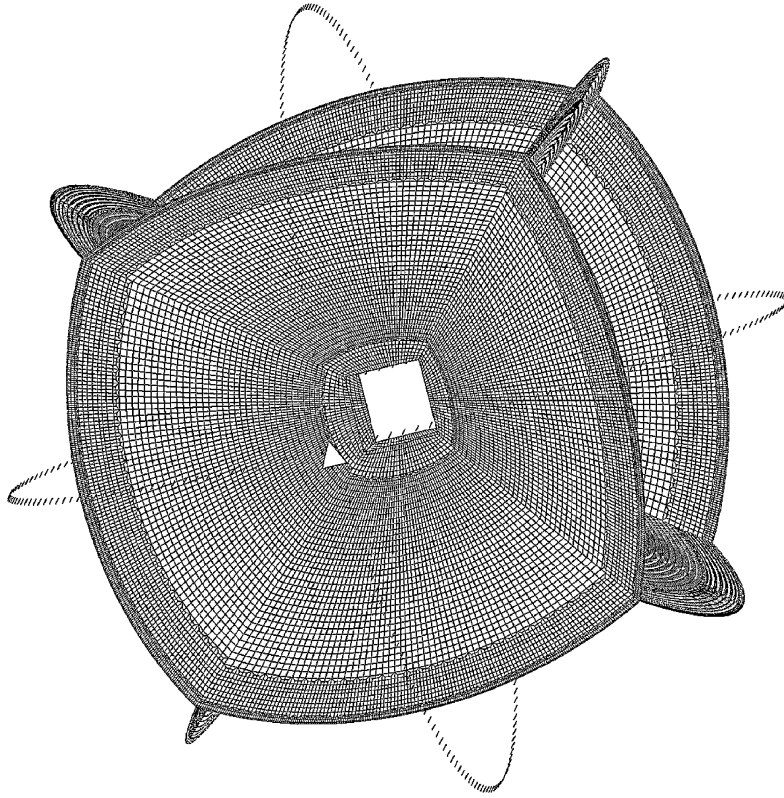
(b)

Figure 6. (a) Mesh used for the simulations presented in this study. It honors first-order discontinuities at depths of 24.4 km, 220 km, 400 km, and 670 km, the CMB, and the ICB; it also honours second-order discontinuities at 600 km, 771 km, and at the top of D''. The mesh is doubled in size once below the Moho, a second time below the 670 km discontinuity, and a third time just above the ICB. Each of the six chunks has 240×240 elements at the free surface and 30×30 elements at the ICB. The triangle indicates the location of the source, situated on the equator and the Greenwich meridian. Rings of receivers with a $2°$ spacing along the equator and the Greenwich meridian are shown by the dashes. We also show a close-up of the two mesh doublings in the mantle (b) .

3   THE SPECTRAL-ELEMENT METHOD

In this article we ignore the effects of self-gravitation and rotation on global wave propagation. Self-gravitation and rotation are only relevant in the context of long-period surface waves and will be considered in a subsequent article (Komatitsch & Tromp 2002).

3.1   Mantle and Crust

The wave equation for the Earth's mantle and crust may be written in the form

$$\rho \partial_t^2 \mathbf{s} = \nabla \cdot \mathbf{T} + \mathbf{f}, \tag{5}$$

where ρ denotes the 3-D distribution of density and $\mathbf{T}$ the stress tensor which is linearly related to the displacement gradient $\nabla\mathbf{s}$ by Hooke's law:

$$\mathbf{T} = \mathbf{c} : \nabla\mathbf{s}. \tag{6}$$

In a transversely isotropic earth model, such as PREM, the elastic tensor $\mathbf{c}$ is determined in terms of the five elastic parameters A, C, L, N, and F (Love 1911).

In an attenuating medium, Hooke's law (eq. 6) needs to be modified such that the stress is determined by the entire strain history:

$$\mathbf{T}(t) = \int_{-\infty}^{t} \partial_t \mathbf{c}(t - t') : \nabla\mathbf{s}(t') \, dt'. \tag{7}$$

In seismology, the quality factor Q is observed to be constant over a wide range of frequencies. Such an absorption-band solid may

be mimicked by a series of L standard linear solids (Liu *et al.* 1976; Carcione *et al.* 1988; Moczo *et al.* 1997). In practice, two or three linear solids usually suffice to obtain an almost constant Q (Emmerich & Korn 1987). Attenuation in the Earth is mainly controlled by the shear quality factor, such that only the time dependence of the isotropic shear modulus needs to be accommodated (the bulk quality factor is several hundred times larger than the shear quality factor throughout the Earth). In a transversely isotropic earth model one keeps track of the time dependence of the effective shear modulus. The shear modulus of such a standard linear solid may be written in the form (Liu *et al.* 1976)

$$\mu(t) = \mu_R \left[1 - \sum_{\ell=1}^{L} \left(1 - \tau_\ell^\epsilon / \tau_\ell^\sigma \right) e^{-t/\tau_\ell^\sigma} \right] H(t). \tag{8}$$

Here μ_R denotes the relaxed modulus, $H(t)$ is the Heaviside function and τ_ℓ^σ and τ_ℓ^ϵ denote the stress and strain relaxation times, respectively, of the ℓth standard linear solid. Using the absorption-band shear modulus (eq. 8), the constitutive relation (eq. 7) may be rewritten in the form

$$\mathbf{T} = \mathbf{c}_U : \nabla\mathbf{s} - \sum_{\ell=1}^{L} \mathbf{R}_\ell, \tag{9}$$

where $\mathbf{c}_U$ is the unrelaxed elastic tensor determined by the unrelaxed shear modulus

$$\mu_U = \mu_R \left[1 - \sum_{\ell=1}^{L} \left(1 - \tau_\ell^\epsilon / \tau_\ell^\sigma \right) \right]. \tag{10}$$

For each standard linear solid one needs to solve the memory-variable equation

$$\partial_t \mathbf{R}_\ell = -(\mathbf{R}_\ell - \delta\mu_\ell \mathbf{D})/\tau_\ell^\sigma, \tag{11}$$

where $\mathbf{D}$ is the strain deviator:

$$\mathbf{D} = \tfrac{1}{2}[\nabla\mathbf{s} + (\nabla\mathbf{s})^T] - \tfrac{1}{3}(\nabla \cdot \mathbf{s})\mathbf{I}. \tag{12}$$

Here a superscript T denotes the transpose and $\mathbf{I}$ is the identity tensor. The memory-variable tensors $\mathbf{R}_\ell$ are symmetric and have zero trace, such that each standard linear solid introduces five additional unknowns. The modulus defect $\delta\mu_\ell$ associated with each individual standard linear solid is determined by

$$\delta\mu_\ell = -\mu_R\left(1 - \tau_\ell^\epsilon/\tau_\ell^\sigma\right). \tag{13}$$

The earthquake source is represented by a point force $\mathbf{f}$, which may be written in terms of the moment tensor $\mathbf{M}$ as

$$\mathbf{f} = -\mathbf{M} \cdot \nabla\delta(\mathbf{r} - \mathbf{r}_s)S(t). \tag{14}$$

The location of the point source is denoted by $\mathbf{r}_s$, $\delta(\mathbf{r} - \mathbf{r}_s)$ denotes the Dirac delta distribution located at $\mathbf{r}_s$, and the source-time function is given by $S(t)$.

Two types of boundary conditions must be considered: on the free surface the traction $\hat{\mathbf{n}} \cdot \mathbf{T}$, where $\hat{\mathbf{n}}$ denotes the unit outward normal on the free surface, vanishes, and on the CMB the normal component of velocity $\hat{\mathbf{n}} \cdot \mathbf{v}$ and the traction $\hat{\mathbf{n}} \cdot \mathbf{T}$ are continuous.

Finite-difference and pseudospectral methods are based upon the equation of motion (eq. 5) subject to the appropriate boundary conditions, which is a differential or 'strong' formulation of the problem. Spectral-element methods, like finite-element, coupled-mode, and direct-solution methods, are based upon an integral or 'weak' formulation of the problem. This formulation is obtained by taking the dot product of the momentum equation (eq. 5) with an arbitrary vector $\mathbf{w}$, called a test vector in the finite-element literature, integrating by parts over the volume M of the mantle and crust and imposing the stress-free boundary condition. This gives

$$\int_M \rho\mathbf{w} \cdot \partial_t^2\mathbf{s}\, d^3\mathbf{r} = -\int_M \nabla\mathbf{w} : \mathbf{T}\, d^3\mathbf{r} + \mathbf{M} : \nabla\mathbf{w}(\mathbf{r}_s)S(t)$$
$$-\int_{CMB} \mathbf{w} \cdot \mathbf{T} \cdot \hat{\mathbf{n}}\, d^2\mathbf{r}, \tag{15}$$

where $\hat{\mathbf{n}}$ is the unit outward normal on the CMB. Eq. (15) is equivalent to the strong formulation (eq. 5) subject to the appropriate boundary conditions because it holds for any test vector $\mathbf{w}$.

The weak formulation (eq. 15) is valid for a completely general, anelastic, anisotropic model. To correctly model interactions between the solid mantle and the fluid core, we need to impose the continuity of traction and of the normal velocity at the CMB. Coupling fluid and solid finite elements is not an easy problem numerically (e.g. Thompson & Pinsky 1996; Bermúdez *et al.* 1999). In this study we implement the fluid–solid interactions based upon a domain decomposition method: in the mantle we impose the continuity of traction and in the next section on the fluid outer core we will impose the continuity of normal velocity. To impose continuity of traction, we replace the traction term $\hat{\mathbf{n}} \cdot \mathbf{T}$ in the integral over the CMB by the traction $-p\hat{\mathbf{n}}$ in the fluid, where p denotes the fluid pressure. We find

$$\int_M \rho\mathbf{w} \cdot \partial_t^2\mathbf{s}\, d^3\mathbf{r} = -\int_M \nabla\mathbf{w} : \mathbf{T}\, d^3\mathbf{r} + \mathbf{M} : \nabla\mathbf{w}(\mathbf{r}_s)S(t)$$
$$+\int_{CMB} p\hat{\mathbf{n}} \cdot \mathbf{w}\, d^2\mathbf{r}. \tag{16}$$

3.2 Outer core

In the fluid outer core, the equation of motion is

$$\rho\partial_t\mathbf{v} = -\nabla p, \tag{17}$$

where $\mathbf{v}$ denotes the velocity in the fluid and the pressure p is determined by

$$\partial_t p = -\kappa\nabla \cdot \mathbf{v}, \tag{18}$$

where κ is the adiabatic bulk modulus of the fluid. On the CMB and the ICB the traction $-p\hat{\mathbf{n}}$ and the normal component of velocity $\hat{\mathbf{n}} \cdot \mathbf{v}$ must be continuous.

To solve the system of eqs (17) and (18), we introduce a scalar potential χ (e.g. Everstine 1981; Kallivokas & Bielak 1993; Lesieur 1997) such that

$$p = -\partial_t\chi. \tag{19}$$

From eq. (17) and the initial conditions ($\mathbf{v} = \mathbf{0}$ at $t = 0$), we find that

$$\mathbf{v} = \rho^{-1}\nabla\chi. \tag{20}$$

Upon substituting eqs (19) and (20) into eq. (18) we obtain a scalar equation for χ:

$$\kappa^{-1}\partial_t^2\chi = \nabla \cdot (\rho^{-1}\nabla\chi). \tag{21}$$

The weak form of this equation is obtained by multiplying it by a scalar test function w and integrating by parts over the volume OC of the outer core:

$$\int_{OC} \kappa^{-1}w\partial_t^2\chi\, d^3\mathbf{r} = -\int_{OC} \rho^{-1}\nabla w \cdot \nabla\chi\, d^3\mathbf{r} + \int_{CMB} w\hat{\mathbf{n}} \cdot \mathbf{v}\, d^2\mathbf{r}$$
$$-\int_{ICB} w\hat{\mathbf{n}} \cdot \mathbf{v}\, d^2\mathbf{r}, \tag{22}$$

where we used eq. (20) in the surface integrals over the CMB and ICB. Again $\hat{\mathbf{n}}$ is the unit outward normal on either the CMB or the ICB.

Komatitsch *et al.* (2000a) used a fluid–solid domain decomposition approach that is valid for homogeneous fluids. The weak formulation, eq. (22), is valid for general, inhomogeneous fluids. At the CMB and the ICB we need to implement the second step of our domain decomposition technique by imposing the continuity of normal velocity. The continuity of traction has already been imposed in eq. (16). At this point we replace the normal component of velocity $\hat{\mathbf{n}} \cdot \mathbf{v}$ in the integrals over the CMB and ICB with the normal component of velocity $\hat{\mathbf{n}} \cdot \partial_t\mathbf{s}$ in the mantle or inner core to represent the interactions correctly:

$$\int_{OC} \kappa^{-1}w\partial_t^2\chi\, d^3\mathbf{r} = -\int_{OC} \rho^{-1}\nabla w \cdot \nabla\chi\, d^3\mathbf{r} + \int_{CMB} w\hat{\mathbf{n}} \cdot \partial_t\mathbf{s}\, d^2\mathbf{r}$$
$$-\int_{ICB} w\hat{\mathbf{n}} \cdot \partial_t\mathbf{s}\, d^2\mathbf{r}. \tag{23}$$

Note that the system of eqs (16) and (23) honours both the continuity of traction and of the normal component of velocity and therefore correctly represents the fluid–solid interactions. This is the key motivation behind our domain decomposition approach.

3.3 Inner core

The weak form of the equation of motion in the solid inner core is similar to eq. (16):

$$\int_{IC} \rho\mathbf{w} \cdot \partial_t^2\mathbf{s}\, d^3\mathbf{r} = -\int_{IC} \nabla\mathbf{w} : \mathbf{T}\, d^3\mathbf{r} - \int_{ICB} p\hat{\mathbf{n}} \cdot \mathbf{w}\, d^2\mathbf{r}. \tag{24}$$

Note that the inner core–outer core interactions, represented by the surface integrals over the ICB in eqs (23) and (24), also honour

continuity in traction and continuity of the normal component of velocity. The normal follows the same convention as in previous sections.

3.4 Interpolation on an element

The next step is to represent the displacement field on an element, which requires the introduction of grid points in each element. In traditional finite-element methods the same low-degree polynomials used to describe the geometry of an element are also used to represent functions, such as the displacement field $\mathbf{s}$, on an element. Spectral-element methods also use a low-degree polynomial to describe the shape of an element, but employ a higher-degree polynomial to represent functions. In this regard, SEMs are related to so-called *h-p* finite-element methods, which also use polynomials of higher degree (e.g. Guo & Babuška 1086). Typically, a SEM uses Lagrange polynomials of degree 4 to 10 for the interpolation of functions (Seriani & Priolo 1994). The $n + 1$ Lagrange polynomials of degree n are defined in terms of $n + 1$ control points $-1 \leq \xi_\alpha \leq 1$, $\alpha = 0, \ldots, n$, by

$$\ell_\alpha^n(\xi) = \frac{(\xi - \xi_0) \cdots (\xi - \xi_{\alpha-1})(\xi - \xi_{\alpha+1}) \cdots (\xi - \xi_n)}{(\xi_\alpha - \xi_0) \cdots (\xi_\alpha - \xi_{\alpha-1})(\xi_\alpha - \xi_{\alpha+1}) \cdots (\xi_\alpha - \xi_n)}. \quad (25)$$

As a result of this definition, the Lagrange polynomials return a value of either zero or one when evaluated at a control point:

$$\ell_\alpha^n(\xi_\beta) = \delta_{\alpha\beta}, \quad (26)$$

where δ denotes the Kronecker delta. In a SEM, the control points ξ_α, $\alpha = 0, \ldots, n$, needed in the definition eq. (25) are chosen to be the $n + 1$ Gauss–Lobatto–Legendre points, which are the roots of $(1 - \xi^2)P_n'(\xi) = 0$, where P_n' denotes the derivative of the Legendre polynomial of degree n (Canuto *et al.* 1988, p. 61). The reason for this choice is that, as we shall see, the combination of Lagrange interpolants with Gauss–Lobatto–Legendre quadrature greatly simplifies the algorithm, in particular regarding time-marching, since it leads to a diagonal mass matrix and therefore to fully explicit time schemes.

Functions f on an element are interpolated in terms of triple products of Lagrange polynomials as

$$f(\mathbf{x}(\xi, \eta, \zeta)) \approx \sum_{\alpha, \beta, \gamma = 0}^{n_\alpha, n_\beta, n_\gamma} f^{\alpha\beta\gamma} \ell_\alpha(\xi) \ell_\beta(\eta) \ell_\gamma(\zeta), \quad (27)$$

where $f^{\alpha\beta\gamma} = f(\mathbf{x}(\xi_\alpha, \eta_\beta, \zeta_\gamma))$ denotes the value of the function f at the Gauss–Lobatto–Legendre point $\mathbf{x}(\xi_\alpha, \eta_\beta, \zeta_\gamma)$. We have dropped the superscript n on the Lagrange polynomials to avoid clutter in the notation. Note that, in principle, the method allows for different polynomial degrees, n_α, n_β, n_γ, in each of the three directions ξ, η, ζ.

Using the polynomial representation eq. (27), the gradient of a function, $\nabla f = \sum_{i=1}^3 \hat{\mathbf{x}}_i \partial_i f$, evaluated at the Gauss-Lobatto-Legendre point $\mathbf{x}(\xi_{\alpha'}, \eta_{\beta'}, \zeta_{\gamma'})$, may be written in the form

$$\nabla f(\mathbf{x}(\xi_{\alpha'}, \eta_{\beta'}, \zeta_{\gamma'})) \approx \sum_{i=1}^3 \hat{\mathbf{x}}_i \left[(\partial_i \xi)^{\alpha'\beta'\gamma'} \sum_{\alpha=0}^{n_\alpha} f^{\alpha\beta'\gamma'} \ell_\alpha'(\xi_{\alpha'}) \right.$$
$$+ (\partial_i \eta)^{\alpha'\beta'\gamma'} \sum_{\beta=0}^{n_\beta} f^{\alpha'\beta\gamma'} \ell_\beta'(\eta_{\beta'})$$
$$\left. + (\partial_i \zeta)^{\alpha'\beta'\gamma'} \sum_{\gamma=0}^{n_\gamma} f^{\alpha'\beta'\gamma} \ell_\gamma'(\zeta_{\gamma'}) \right]. \quad (28)$$

Here $\hat{\mathbf{x}}_i$, $i = 1, 2, 3$, denote unit vectors in the directions of increasing x, y, and z, respectively, and ∂_i, $i = 1, 2, 3$, denote partial derivatives in those directions. We use a prime to denote derivatives of the Lagrange polynomials, as in ℓ_α'. The matrix $\partial \boldsymbol{\xi}/\partial \mathbf{x}$ is obtained by inverting the matrix $\partial \mathbf{x}/\partial \boldsymbol{\xi}$. This inverse exists provided the Jacobian J is non-singular, which is a requirement for the proper design of the mesh, as mentioned earlier.

3.5 Integration over an element

To solve the weak form of the equations of motion (16), (23), and (24), numerical integrations over the elements need to be performed. In classical finite-element methods, one frequently uses Gauss quadrature for this purpose. In a spectral-element method, one uses the Gauss–Lobatto–Legendre integration rule, because it leads to a diagonal mass matrix when used in conjunction with the Gauss–Lobatto–Legendre interpolation points, which greatly simplifies the algorithm. Using Gauss–Lobatto–Legendre quadrature, integrations over elements with volume Ω_e may be expressed as

$$\int_{\Omega_e} f(\mathbf{x}) d^3\mathbf{x} = \int_{-1}^1 \int_{-1}^1 \int_{-1}^1 f(\mathbf{x}(\xi, \eta, \zeta)) J(\xi, \eta, \zeta) d\xi d\eta d\zeta$$
$$\approx \sum_{\alpha, \beta, \gamma = 0}^{n_\alpha, n_\beta, n_\gamma} \omega_\alpha \omega_\beta \omega_\gamma f^{\alpha\beta\gamma} J^{\alpha\beta\gamma}, \quad (29)$$

where $J^{\alpha\beta\gamma} = J(\xi_\alpha, \eta_\beta, \zeta_\gamma)$, and $\omega_\alpha > 0$, for $\alpha = 0, \ldots, n$, denote the weights associated with the Gauss–Lobatto–Legendre quadrature (Canuto *et al.* 1988, p. 61). To perform this integration of functions and their partial derivatives over the elements, the values of the inverse Jacobian matrix $\partial \boldsymbol{\xi}/\partial \mathbf{x}$ need to be computed at the $(n + 1)^3$ Gauss–Lobatto–Legendre integration points.

On the fluid–solid boundaries in the model we need to evaluate surface integrals in order to implement the coupling based upon domain decomposition. At the elemental level, using Gauss–Lobatto–Legendre quadrature, these surface integrations may be written in the form

$$\int_{\Gamma_b} f(\mathbf{x}) d^2\mathbf{x} = \int_{-1}^1 \int_{-1}^1 f(\mathbf{x}(\xi, \eta)) J_b(\xi, \eta) d\xi d\eta$$
$$\approx \sum_{\alpha, \beta = 0}^{n_\alpha, n_\beta} \omega_\alpha \omega_\beta f^{\alpha\beta} J_b^{\alpha\beta}, \quad (30)$$

where Γ_b denotes the surface element, and $J_b^{\alpha\beta} = J_b(\xi_\alpha, \eta_\beta)$ is the Jacobian eq. (4) evaluated at the Gauss–Lobatto–Legendre points of integration.

3.6 Discretization of the weak formulation

To obtain explicit expressions for the weak formulation of the problem, we first expand the displacement field $\mathbf{s}$ and the test vector $\mathbf{w}$ in terms of Lagrange polynomials:

$$\mathbf{s}(\mathbf{x}(\xi, \eta, \zeta), t) \approx \sum_{i=1}^3 \hat{\mathbf{x}}_i \sum_{\sigma, \tau, \nu = 0}^{n_\sigma, n_\tau, n_\nu} s_i^{\sigma\tau\nu}(t) \ell_\sigma(\xi) \ell_\tau(\eta) \ell_\nu(\zeta), \quad (31)$$

$$\mathbf{w}(\mathbf{x}(\xi, \eta, \zeta)) = \sum_{i=1}^3 \hat{\mathbf{x}}_i \sum_{\alpha, \beta, \gamma = 0}^{n_\sigma, n_\tau, n_\nu} w_i^{\alpha\beta\gamma} \ell_\alpha(\xi) \ell_\beta(\eta) \ell_\gamma(\zeta). \quad (32)$$

This choice of test vector makes the SEM a Galerkin method, because the basis functions are the same as those used to represent

the displacement. We evaluate the integrals in eqs (16), (23) and (24) at the elemental level based upon Gauss–Lobatto–Legendre quadrature. The term on the left hand side of the weak form of the equation of motion (16) is traditionally called the *mass matrix* in finite-element modelling. At the elemental level, this integration may be written as

$$\int_{\Omega_e} \rho \mathbf{w} \cdot \partial_t^2 \mathbf{s} \, d^3\mathbf{x} = \int_{-1}^{1} \int_{-1}^{1} \int_{-1}^{1} \rho(\mathbf{x}(\boldsymbol{\xi})) \mathbf{w}(\mathbf{x}(\boldsymbol{\xi})) \\ \cdot \partial_t^2 \mathbf{s}(\mathbf{x}(\boldsymbol{\xi}), t) \, J(\boldsymbol{\xi}) \, d^3\boldsymbol{\xi}. \tag{33}$$

Upon substituting the interpolations eqs (31) and 32 in eq. (33), using the quadrature eq. (29), we obtain

$$\int_{\Omega_e} \rho \mathbf{w} \cdot \partial_t^2 \mathbf{s} \, d^3\mathbf{x} \approx \sum_{\alpha,\beta,\gamma=0}^{n_\alpha,n_\beta,n_\gamma} \omega_\alpha \omega_\beta \omega_\gamma J^{\alpha\beta\gamma} \rho^{\alpha\beta\gamma} \sum_{i=1}^{3} w_i^{\alpha\beta\gamma} \ddot{s}_i^{\alpha\beta\gamma}(t), \tag{34}$$

where $\rho^{\alpha\beta\gamma} = \rho(\mathbf{x}(\xi_\alpha, \eta_\beta, \zeta_\gamma))$, and where a dot denotes differentiation with respect to time. By independently setting factors of $w_1^{\alpha\beta\gamma}$, $w_2^{\alpha\beta\gamma}$ and $w_3^{\alpha\beta\gamma}$ equal to zero, as the weak formulation eq. (15) must hold for any test vector $\mathbf{w}$, we obtain independent equations for each component of acceleration $\ddot{s}_i^{\alpha\beta\gamma}(t)$ at grid point $(\xi_\alpha, \eta_\beta, \gamma_\beta)$. The remarkable property of eq. (34) is that the value of acceleration at each point of a given element, $\ddot{s}_i^{\alpha\beta\gamma}(t)$, is simply multiplied by the factor $\omega_\alpha \omega_\beta \omega_\gamma \rho^{\alpha\beta\gamma} J^{\alpha\beta\gamma}$. In finite-element parlance one says that the elemental mass matrix is diagonal. It is this desirable property that has motivated the use of Lagrange interpolants together with Gauss–Lobatto–Legendre quadrature. Unlike in traditional finite-element methods, no linear system of equations needs to be inverted, and one can take full advantage of this property by using an explicit time-marching algorithm, as we will see later in this section. This is similar to the key idea used in finite-element methods with mass lumping (e.g. Cohen *et al.* 1993; Bao *et al.* 1998).

The next integral that needs to be evaluated at the elemental level is the first term on the right hand side of eq. (16), which is called the stiffness matrix in finite-element modelling. We find

$$\int_{\Omega_e} \nabla \mathbf{w} : \mathbf{T} \, d^3\mathbf{x} \approx \sum_{\alpha,\beta,\gamma=0}^{n_\alpha,n_\beta,n_\gamma} \sum_{i=1}^{3} w_i^{\alpha\beta\gamma} \\ \times \left[\omega_\beta \omega_\gamma \sum_{\alpha'=0}^{n_{\alpha'}} \omega_{\alpha'} J_e^{\alpha'\beta\gamma} F_{i1}^{\alpha'\beta\gamma} \ell'_\alpha(\xi_{\alpha'}) \right. \\ + \omega_\alpha \omega_\gamma \sum_{\beta'=0}^{n_{\beta'}} \omega_{\beta'} J_e^{\alpha\beta'\gamma} F_{i2}^{\alpha\beta'\gamma} \ell'_\beta(\eta_{\beta'}) \\ \left. + \omega_\alpha \omega_\beta \sum_{\gamma'=0}^{n_{\gamma'}} \omega_{\gamma'} J_e^{\alpha\beta\gamma'} F_{i3}^{\alpha\beta\gamma'} \ell'_\gamma(\zeta_{\gamma'}) \right] \tag{35}$$

where

$$F_{ik} = \sum_{j=1}^{3} T_{ij} \partial_j \xi_k, \tag{36}$$

and $F_{ik}^{\sigma\tau\nu} = F_{ik}(\mathbf{x}(\xi_\sigma, \eta_\tau, \zeta_\nu))$ denotes the value of F_{ik} at the Gauss–Lobatto–Legendre integration point $\mathbf{x}(\xi_\sigma, \eta_\tau, \zeta_\nu)$. For brevity, we have introduced index notation ξ_i, $i = 1, 2, 3$, where $\xi_1 = \xi$, $\xi_2 = \eta$, and $\xi_3 = \zeta$. In index notation, the elements of the mapping matrix $\partial \boldsymbol{\xi}/\partial \mathbf{x}$ may be written as $\partial_i \xi_j$. The value of the stress tensor $\boldsymbol{T}$ at the integration points is determined by

$$\mathbf{T}(\mathbf{x}(\xi_\alpha, \eta_\beta, \zeta_\gamma), t) = \mathbf{c}(\mathbf{x}(\xi_\alpha, \eta_\beta, \zeta_\gamma)) : \nabla \mathbf{s}(\mathbf{x}(\xi_\alpha, \eta_\beta, \zeta_\gamma), t). \tag{37}$$

This calculation requires knowledge of the gradient of displacement $\nabla \mathbf{s}$ at the Gauss–Lobatto–Legendre integration points. Upon differentiating eq. (31) we obtain

$$\partial_i s_j(\mathbf{x}(\xi_\alpha, \eta_\beta, \zeta_\gamma), t) = \left[\sum_{\sigma=0}^{n_\sigma} s_j^{\sigma\beta\gamma}(t) \ell'_\sigma(\xi_\alpha) \right] \partial_i \xi(\xi_\alpha, \eta_\beta, \zeta_\gamma) \\ + \left[\sum_{\sigma=0}^{n_\sigma} s_j^{\alpha\sigma\gamma}(t) \ell'_\sigma(\eta_\beta) \right] \partial_i \eta(\xi_\alpha, \eta_\beta, \zeta_\gamma) \\ + \left[\sum_{\sigma=0}^{n_\sigma} s_j^{\alpha\beta\sigma}(t) \ell'_\sigma(\zeta_\gamma) \right] \partial_i \zeta(\xi_\alpha, \eta_\beta, \zeta_\gamma). \tag{38}$$

In an anelastic medium, the stiffness matrix is still given by eq. (35), except that the stress tensor eq. (37) needs to be replaced by

$$\mathbf{T}(\mathbf{x}(\xi_\alpha, \eta_\beta, \zeta_\gamma), t) = \mathbf{c}(\mathbf{x}(\xi_\alpha, \eta_\beta, \zeta_\gamma)) : \nabla \mathbf{s}(\mathbf{x}(\xi_\alpha, \eta_\beta, \zeta_\gamma), t) \\ - \sum_{\ell=1}^{L} \mathbf{R}_\ell(\mathbf{x}(\xi_\alpha, \eta_\beta, \zeta_\gamma), t), \tag{39}$$

in accordance with eq. (9). The implication is that the five independent components of the symmetric, zero-trace memory tensor $\mathbf{R}_\ell$ need to be stored on the grid for each standard linear solid. For this reason, the memory requirements for an anelastic simulation increase substantially over those for purely elastic simulations. It is worth mentioning that to alleviate this burden, memory variables could be spread across an element, such that one carries only one memory variable at each gridpoint, obtaining the expected anelastic behaviour in average (Zeng 1996; Day 1998).

The second term on the right hand side of the weak form of the equation of motion in the mantle, eq. (16), is the source term, which may be expressed as (Komatitsch & Tromp 1999)

$$\mathbf{M} : \nabla \mathbf{w}(\mathbf{x}_s) \approx \sum_{\alpha,\beta,\gamma=0}^{n_\alpha,n_\beta,n_\gamma} \sum_{i=1}^{3} w_i^{\alpha\beta\gamma} \left\{ \sum_{\sigma,\tau,\nu=0}^{n_\sigma,n_\tau,n_\nu} \ell_\sigma(\xi_{\alpha_s}) \ell_\tau(\eta_{\beta_s}) \ell_\nu(\zeta_{\gamma_s}) \right. \\ \times \left[G_{i1}^{\sigma\tau\nu} \ell'_\alpha(\xi_{\alpha_s}) \ell_\beta(\eta_{\beta_s}) \ell_\gamma(\zeta_{\gamma_s}) \right. \\ + G_{i2}^{\sigma\tau\nu} \ell_\alpha(\xi_{\alpha_s}) \ell'_\beta(\eta_{\beta_s}) \ell_\gamma(\zeta_{\beta_s}) \\ \left. \left. + G_{i3}^{\sigma\tau\nu} \ell_\alpha(\xi_{\alpha_s}) \ell_\beta(\eta_{\beta_s}) \ell'_\gamma(\zeta_{\gamma_s}) \right] \right\}, \tag{40}$$

where

$$G_{ik} = \sum_{j=1}^{3} M_{ij} \partial_j \xi_k, \tag{41}$$

and where $G_{ik}^{\sigma\tau\nu} = G_{ik}(\mathbf{x}(\xi_\sigma, \eta_\tau, \zeta_\nu))$ and $\mathbf{x}(\xi_{\alpha_s}, \eta_{\beta_s}, \zeta_{\gamma_s}) = \mathbf{x}_s$. Note that, due to the polynomial expansion, a point moment-tensor source gets spread over the entire element that contains the point source. This is not a problem, since the expression is consistent with the polynomial basis, except if receivers are placed very close to the source, particularly within the same element (Faccioli *et al.* 1997). Note also that the location of the source does not need to correspond to a Gauss–Lobatto–Legendre grid point.

The final term on the right hand side of the weak form of the equation of motion in the mantle and crust, eq. (16) is the surface integral over the CMB that represents the interactions in traction between the solid mantle and the liquid core. A key ingredient of our domain decomposition technique is that, since we have a conforming mesh everywhere, i.e. the grid points on the CMB are common to the meshes in the mantle and in the outer core, we can take

the value of pressure at a given grid point from the fluid side, and use it directly in the surface integral on the solid side. Therefore, no interpolation is needed at a fluid–solid interface. This type of matching is referred to as pointwise matching in the finite-element literature. At the elemental level on a boundary, the surface integral may therefore be expressed as

$$\int_{\Gamma_b} p\hat{\mathbf{n}} \cdot \mathbf{w} \, d^2\mathbf{r} \approx \sum_{\alpha,\beta=0}^{n_\alpha,n_\beta} \omega_\alpha \omega_\beta J_b^{\alpha\beta} \dot{\chi}^{\alpha\beta}(t) \sum_{i=1}^{3} w_i^{\alpha\beta} \hat{n}_i^{\alpha\beta}, \tag{42}$$

where we have used eq. (19).

In the fluid outer core, the left hand side of the weak form of the equation of motion, eq. (23), may be written at the elemental level in the form

$$\int_{\Omega_e} \kappa^{-1} w \partial_t^2 \chi \, d^3\mathbf{r} \approx \sum_{\alpha,\beta,\gamma=0}^{n_\alpha,n_\beta,n_\gamma} \omega_\alpha \omega_\beta \omega_\gamma J^{\alpha\beta\gamma} (\kappa^{\alpha\beta\gamma})^{-1} w^{\alpha\beta\gamma} \ddot{\chi}^{\alpha\beta\gamma}(t). \tag{43}$$

As for the left hand side of the weak form in the solid regions, eq. (34), this elemental 'mass' matrix is diagonal. The first integral on the right side of the fluid weak formulation, eq. (23) becomes at the elemental level

$$\int_{\Omega_e} \rho^{-1} \nabla w \cdot \nabla \chi \, d^3\mathbf{r}$$

$$\approx \sum_{\alpha,\beta,\gamma=0}^{n_\alpha,n_\beta,n_\gamma} w^{\alpha\beta\gamma} \left[\omega_\beta \omega_\gamma \sum_{\alpha'=0}^{n_{\alpha'}} \omega_{\alpha'} J_e^{\alpha'\beta\gamma} (\rho^{\alpha'\beta\gamma})^{-1} (\partial_1\chi)^{\alpha'\beta\gamma} \ell'_\alpha(\xi_{\alpha'}) \right.$$

$$+ \omega_\alpha \omega_\gamma \sum_{\beta'=0}^{n_{\beta'}} \omega_{\beta'} J_e^{\alpha\beta'\gamma} (\rho^{\alpha\beta'\gamma})^{-1} (\partial_2\chi)^{\alpha\beta'\gamma} \ell'_\beta(\eta_{\beta'})$$

$$+ \left. \omega_\alpha \omega_\beta \sum_{\gamma'=0}^{n_{\gamma'}} \omega_{\gamma'} J_e^{\alpha\beta\gamma'} (\rho^{\alpha\beta\gamma'})^{-1} (\partial_3\chi)^{\alpha\beta\gamma'} \ell'_\gamma(\zeta_{\gamma'}) \right], \tag{44}$$

where

$$(\partial_i\chi)^{\alpha\beta\gamma} = \sum_{\alpha=0}^{n_\alpha} \chi^{\alpha\beta'\gamma'} \ell'_\alpha(\xi_{\alpha'})\partial_i\xi + \sum_{\beta=0}^{n_\beta} \chi^{\alpha'\beta\gamma'} \ell'_\beta(\eta_{\beta'})\partial_i\eta$$

$$+ \sum_{\gamma=0}^{n_\gamma} \chi^{\alpha'\beta'\gamma} \ell'_\gamma(\zeta_{\gamma'})\partial_i\zeta. \tag{45}$$

The remaining volume and surface integrals in eqs (23) and (24) are identical in form to other integrals already discussed in this section.

3.7 Assembly of the system and time marching

In each individual spectral element, functions are sampled at the Gauss–Lobatto–Legendre points of integration. Grid points that lie on the sides, edges, or corners of an hexahedral element are shared amongst neighbouring elements, as illustrated in Fig. 7. Therefore, as in a classical finite-element method, we need to distinguish the local mesh of grid points that define an element from the global mesh of all the grid points in the model, many of which are shared amongst several spectral elements. A mapping between grid points in the local mesh and grid points in the global mesh needs to be defined; efficient routines are available for this purpose from finite-element modelling. Before the system can be marched forward in time, the contributions (the so-called *internal forces*) from all the elements that share a common global grid point need to be summed.
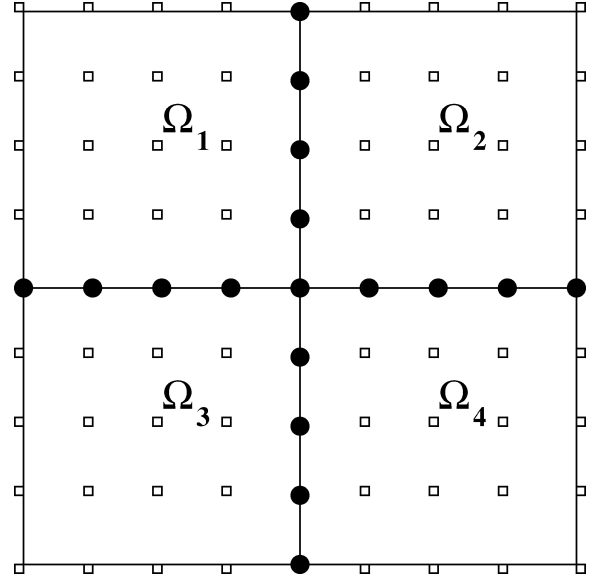

Figure 7. Schematic illustration of the local and global meshes for a four-element 2-D spectral-element discretization with a polynomial degree of $N = 4$. Each element contains $(N + 1)^2 = 25$ Gauss–Lobatto–Legendre points that constitute the local mesh for each element. These points are non-evenly spaced but have been drawn evenly spaced here for simplicity. In the global mesh, points lying on edges or corners (as well as on faces in 3-D) are shared between elements. The contributions to the global system of degrees of freedom, computed separately on each element, have to be summed at the common points represented by black dots. Exactly two elements share points on an edge in 2-D, while corners can be shared by any number of elements depending on the topology of the mesh, which may be non-structured.

In a traditional finite-element method this is referred to as assembling the system. This assembly stage is a costly part of the calculation on parallel computers, because information from individual elements needs to be shared with neighbouring elements. From a computational point of view, this operation involves communications between distinct CPUs.

Let **U** denote the displacement vector of the global system in the solid regions, i.e. **U** contains the displacement vector at all the grid points in the global mesh, classically referred to as the global degrees of freedom of the system. The ordinary differential equation that governs the time dependence of the global system may be written in the form

$$\mathbf{M}\ddot{\mathbf{U}} + \mathbf{K}\mathbf{U} + \mathbf{B}\mathbf{U} = \mathbf{F}, \tag{46}$$

where **M** denotes the global diagonal mass matrix, **K** the global stiffness matrix, **B** the boundary interactions at the CMB or ICB and **F** the source term, all of which have been described at the elemental level earlier in this section. To take full advantage of the fact that the global mass matrix is diagonal, time discretization of the second-order ordinary differential equation (46) is achieved based upon a classical explicit second-order finite-difference scheme, which is a particular case of the more general Newmark scheme (e.g. Hughes 1987), moving the stiffness and boundary terms to the right-hand side. Such a scheme is conditionally stable, and the Courant stability condition is governed by the maximum value of the ratio between the *P*-wave velocity and the size of the grid spacing. In the fluid regions of the model, we solve a system similar to eq. (46) but written in terms of the generalized scalar potential χ. Because of the domain decomposition used to match the fluid and the solid regions of the model, we implement the scheme in a staggered

predictor–multicorrector format (Park & Felippa 1980; Felippa & Deruntz 1984; Thompson & Pinsky 1996; Komatitsch *et al.* 2000a), iterating on the coupling conditions (i.e. the surface integrals over the CMB and the ICB). Such an iterative scheme converges very rapidly (Komatitsch *et al.* 2000a), after only two iterations in practice in the cases presented in this study. The iterations have a negligible impact on the cost of the method since we only need to iterate on the degrees of freedom that are coupled at the interface (i.e. only the layers of elements in contact with the CMB and the ICB, which represent a very small percentage of the total number of elements).

The memory-variable equation, eq. (11), is solved for $\mathbf{R}_\ell$ using a modified second-order Runge–Kutta scheme in time, since such schemes are known to be efficient for this problem (Carcione 1994). We do not spread the memory variables across the grid.

Two quantities that reflect the quality of the mesh are the number of grid points per wavelength, i.e. the resolution of the mesh in terms of how well it samples the wavefield,

$$N = \tau_0 (v/\Delta h)_{\min}, \tag{47}$$

and the stability condition

$$C = \Delta t (v/\Delta h)_{\max}, \tag{48}$$

which illustrates how large the time step of the explicit time integration scheme can be while maintaining a stable simulation. Here τ_0 denotes the shortest period of the source, $(v/\Delta h)_{\min}$ denotes the minimum ratio of wave speed v and grid spacing Δh within a given element, and $(v/\Delta h)_{\max}$ denotes the maximum ratio of wave speed and grid spacing. Fig. 8 illustrates that we maintain a relatively similar number of grid points per wavelength, N, throughout the mesh

shown in Fig. 6, and also shows the stability condition, C, obtained with the time step used in the numerical simulations. This underlines that the mesh coarsening of Fig. 6 used in this article is a simple and efficient solution for meshing the entire Earth.

It is worth mentioning that the two time schemes used in this study are only second-order accurate, contrary to the high-order spatial accuracy provided by the spectral-element discretization. Therefore it might be of interest in the future to switch to higher-order time schemes, as proposed for instance by Tarnow & Simo (1994). However, in the current implementation this problem is not critical since the stability condition of the explicit time scheme imposes a reasonably small time step, which provides an accurate evolution in time, even with a simple second-order scheme.

4 PARALLEL IMPLEMENTATION

The mesh designed for the Earth in Fig. 6 is too large to fit in memory on a single computer. We therefore implement the method on a cluster of PCs using a message-passing programming methodology. Research on how to use large PC clusters for scientific purposes started in 1994 with NASA's Beowulf project, named after the famous Old English poem narrating the adventures of the Scandinavian prince *Beowulf* (e.g. Heaney 2000), later followed by the Hyglac project at Caltech and the Loki project at Los Alamos (Taubes 1996; Sterling *et al.* 1999). The name of the initial project is now used as a generic name for this type of architecture: these PC cluster computers are referred to as 'Beowulf' machines. Clusters are now being used in many fields in academia and industry. Hans-Peter Bunge from Princeton University was among the first to use such clusters to address geophysical problems. Their main advantage is that they
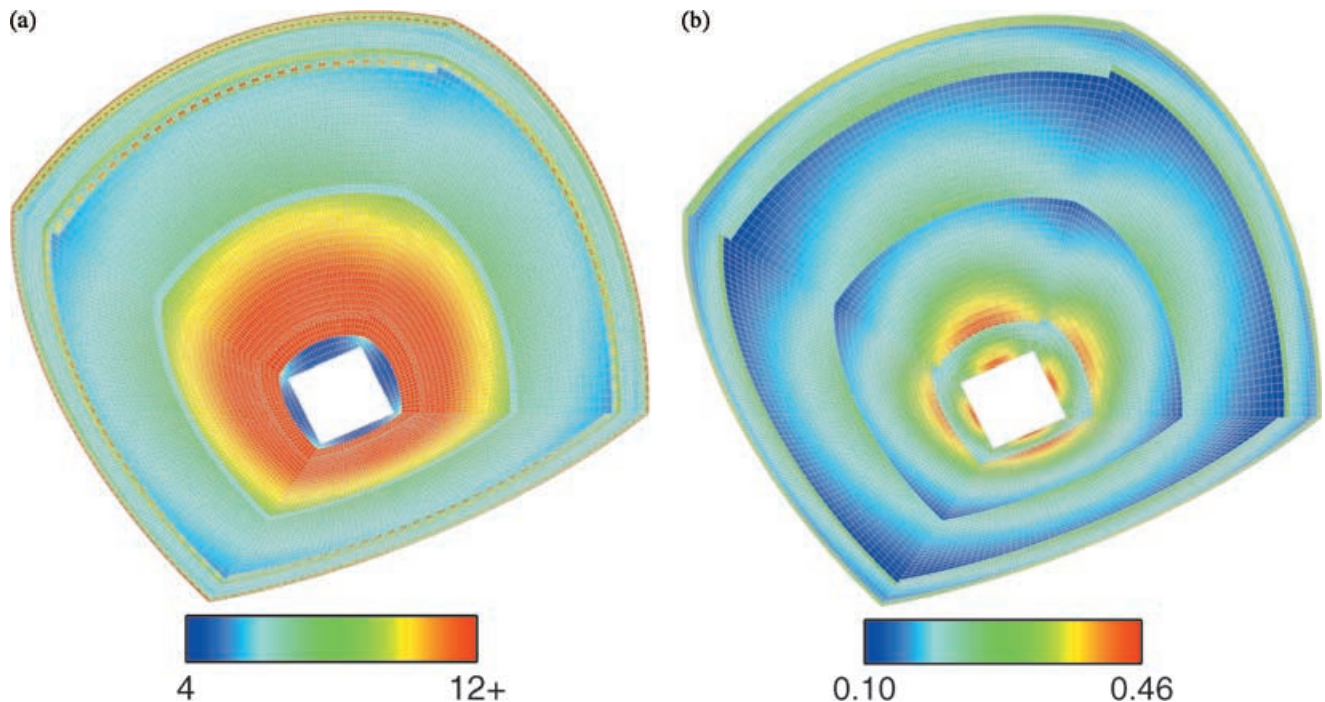

Figure 8. (a) We maintain a relatively similar number of grid points per wavelength, N defined in eq. (47) for a 25 s reference period, throughout the mesh shown in Fig. 6. The color scale indicates the average number of points per wavelength from 4 (dark blue) to 12 or more (red). Note that the doubling region right below the Moho oversamples the wavefield because the size of the elements in the doubling layer is too small relative to the wave speeds. Note also that the number of grid points per wavelength for the inner-core shear wave ($\simeq 4$) is slightly too small since the SEM needs roughly 4.5 points per wavelength to be accurate (Seriani & Priolo 1994). This is acceptable in practice because the inner-core shear wave is a very small phase. (b) Illustration of the stability condition, C defined by eq. (48), throughout the mesh. The stability value goes from 0.10 (dark blue) to 0.46 (red). Note that the size of the time step is controlled by elements in the doubling region just above the ICB, where the stability value has a maximum.
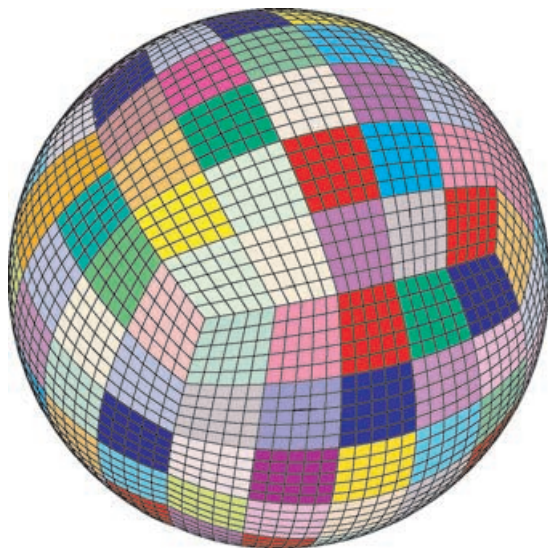
Figure 9. Each of the six chunks that makes up the cubed sphere is subdivided in terms of 25 slices of elements. Each of these slices resides on a single CPU. The central cube is handled by one extra processor, such that the entire calculation involves 151 CPUs. The results on the edges of a slice need to be communicated to all its neighbours. Note that the communication patterns are different for slices inside a chunk, on the edges of a chunk, and on the corners of a chunk.

provide an excellent price-performance ratio, i.e. impressive performance can be reached at relatively low cost compared to classical shared-memory computers. The main drawback of the parallel approach is that one needs to use message-passing techniques, since memory is distributed over the different PCs, which makes the implementation of algorithms usually more difficult. An important advantage, however, is the portability of codes written based upon
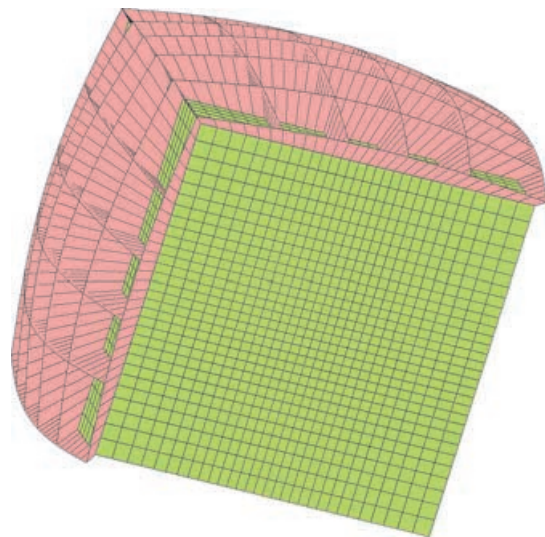
Figure 10. The MPI communication pattern is particularly difficult for the central cube, which is handled by a separate processor that needs to communicate with all the other processors, because every slice of the mesh touches it. Some slices have been removed for clarity. One needs to use a master/slave programming methodology in order to avoid communication patterns that deadlock. In our implementation, the central cube acts as a master to which all the slices, the slaves, report the results of their calculations. The master collects the results from the slices, adds them to his calculations, and sends the results back to the slaves, who update their calculations.
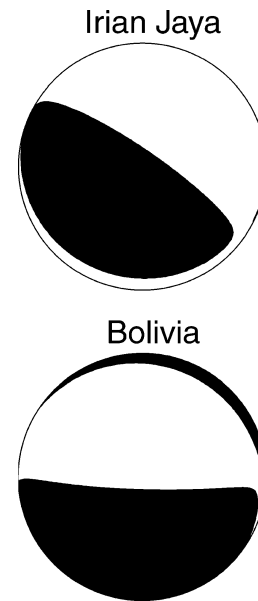

Figure 11. Focal mechanisms for the 1996 February 17 Irian Jaya earthquake which occurred at a depth of 15 km, and the 1994 June 9 Bolivia event which occurred at a depth of 647 km. Both events have a moment magnitude $M_w = 8.2$.
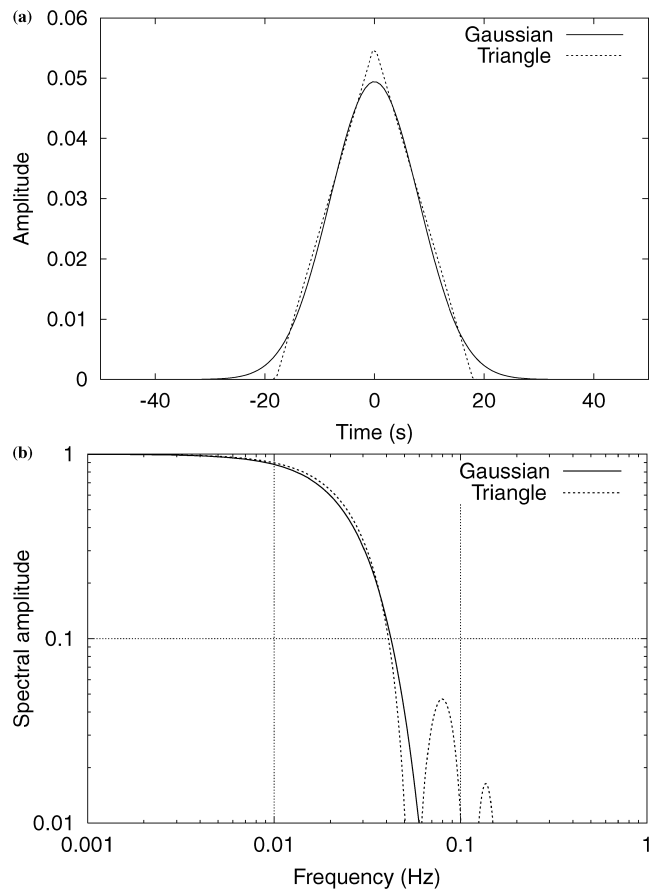

Figure 12. (a) Gaussian source–time function used in the benchmarks between the SEM and normal-mode method (solid line). The source-time function is very similar to a triangle with a half-duration of 18 s (dotted line). (b) Spectral amplitude of the source. Unlike the triangle, the Gaussian source–time function has no significant energy at periods shorter than 20 s.
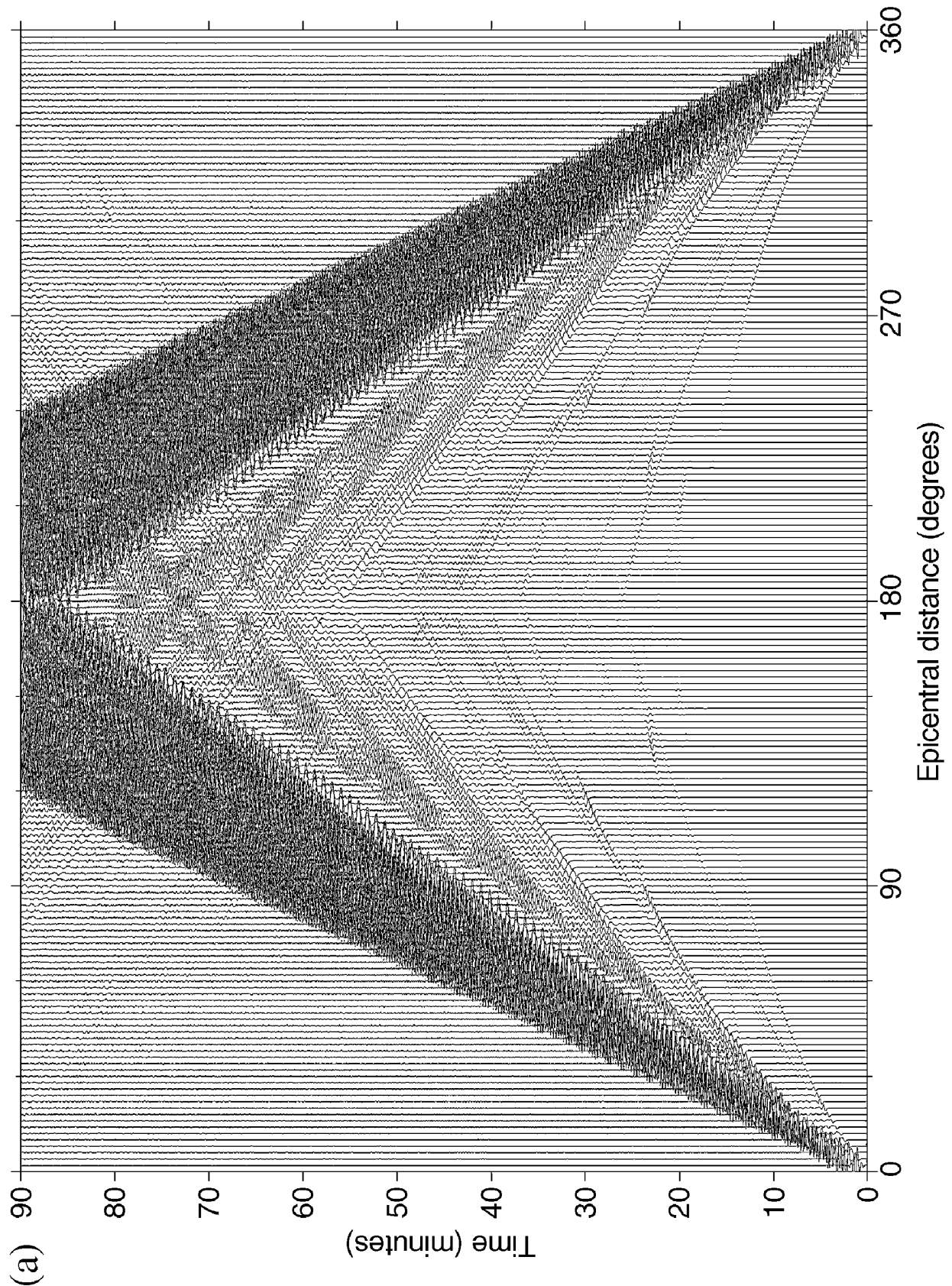
Figure 13. A SEM (solid lines) and normal-mode (dotted lines) record sections for elastic, anisotropic PREM. The event is the 1996 February 17 Irian Jaya earthquake which occurred at a depth of 15 km. Stations record ground displacement at 2° intervals along the equator. Each trace is individually scaled so that they all have the same maximum value. (a) vertical component, (b) radial component and (c) Transverse component. The SEM and normal-mode synthetics are in excellent agreement for all body- and surface-wave arrivals; they almost cannot be distinguished on the scale of this figure.
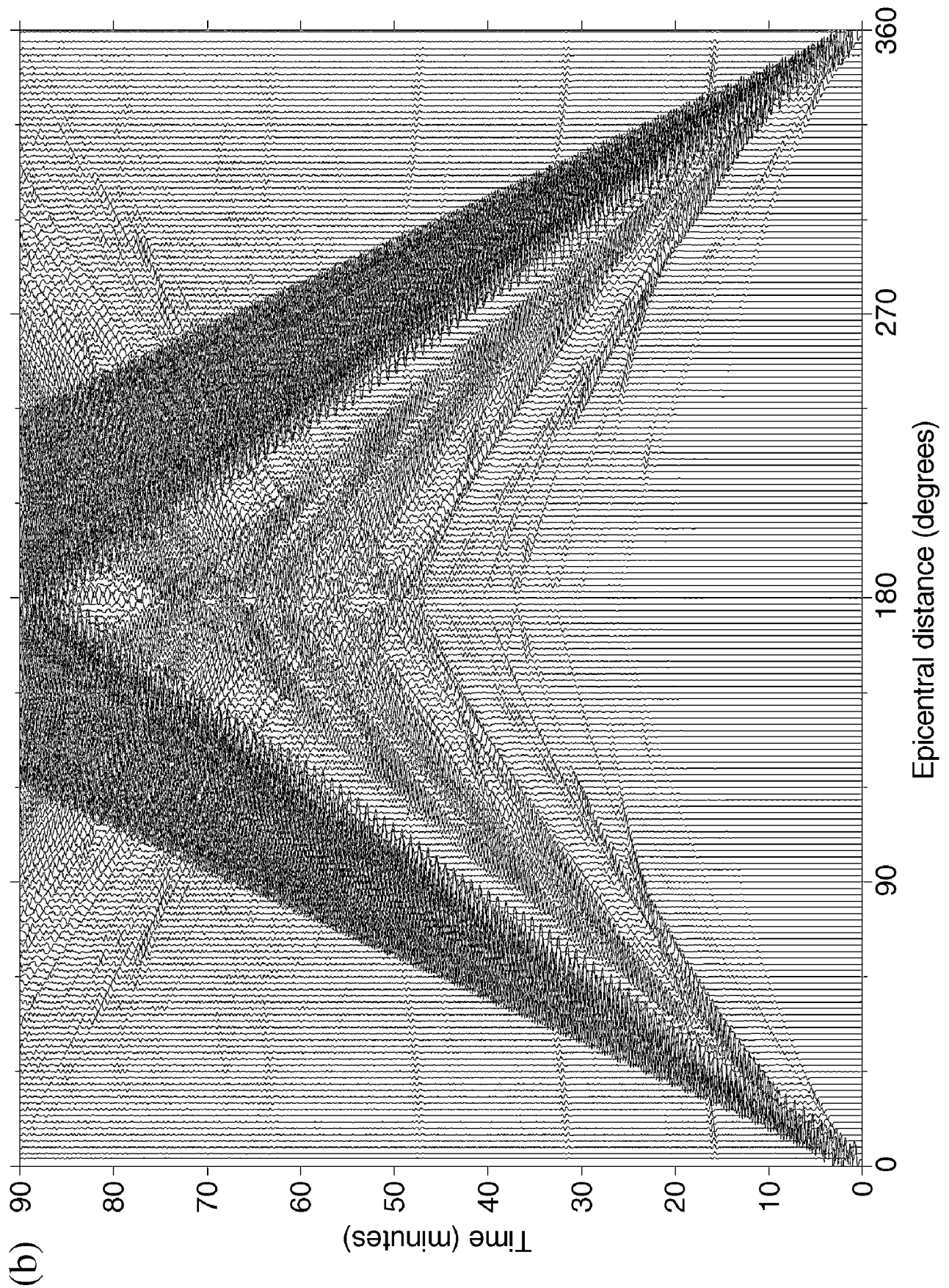
Figure 13. (*Continued.*)
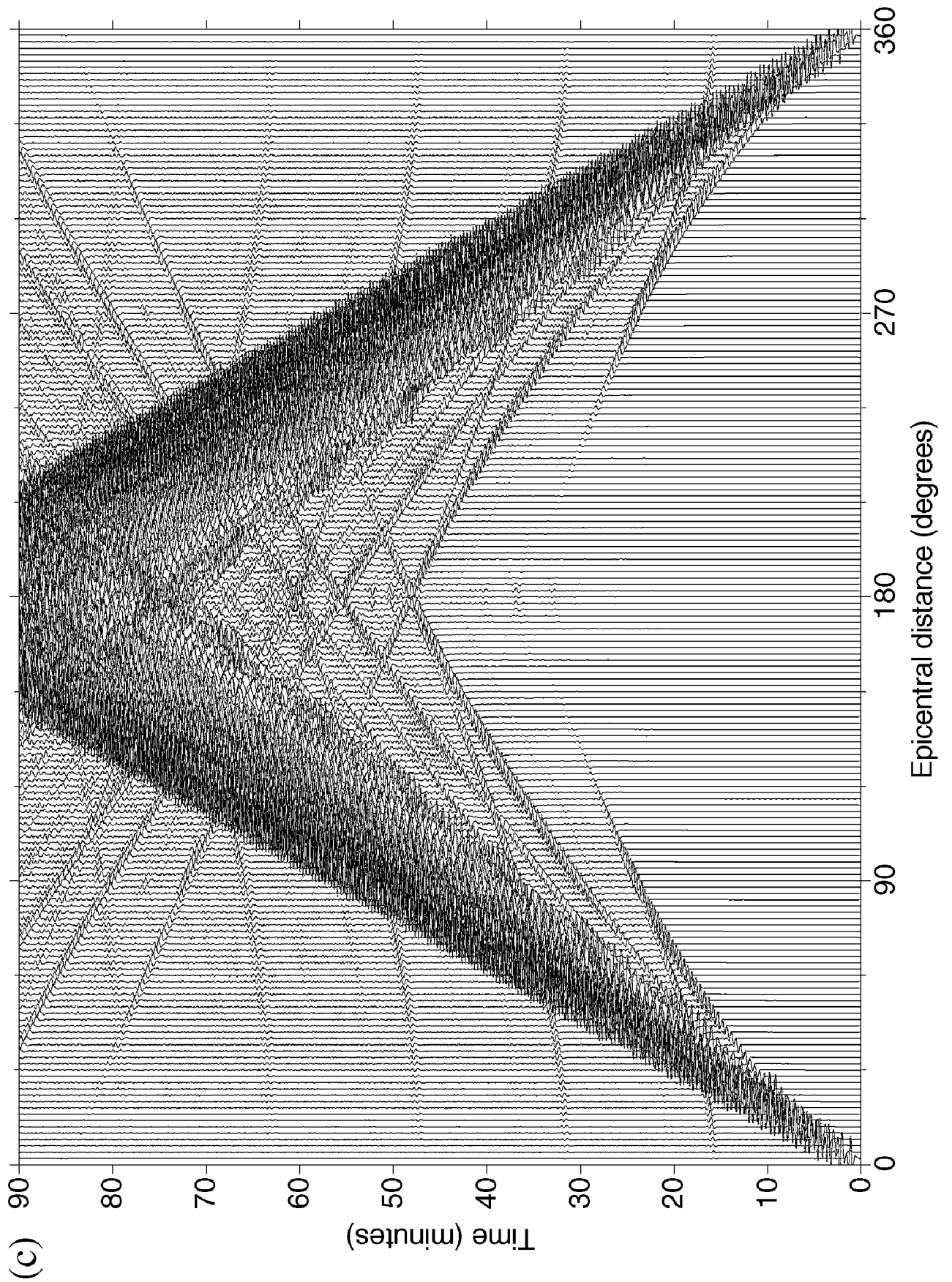
Figure 13. (*Continued.*)

this philosophy, because they can virtually run on any kind of machine, including shared-memory computers.

The standard approach for programming clusters is to use a message-passing library called MPI (e.g. Gropp *et al.* 1994; Pacheco 1997), an acronym for 'Message Passing Interface'. MPI has become a de facto standard in the parallel computing community, thus ensuring the portability of software. More specifically, we use the open-source implementation called MPICH from Argonne National Laboratory (Gropp *et al.* 1996). In our SEM, because we can use fully explicit time-marching schemes since the mass matrix is diagonal by construction, the PCs spend most of their time doing computations, and communications of results between PCs represent only a small fraction of the time of simulation. Therefore, clusters of PCs are ideal for this application in spite of the high latency of the inexpensive 100 Mbits s^{-1} standard Ethernet network connecting them.

The SEM calculations are performed on a PC cluster in the Seismological Laboratory at Caltech. This machine consists of 80 dual-processor PCs with 1 Gb of memory each. The simulations are distributed over 151 processors: each of the six chunks that constitute the globe is subdivided amongst 25 processors (corresponding to 25 mesh slices), and the cube at the centre of the inner core uses one separate processor. Fig. 9 shows how the slices are designed in the cubed-sphere mesh. Note that inside each of the six chunks the mesh of slices is derived from a regular Cartesian topology. However, the topology of the network of slices is different between chunks: each corner of each chunk is shared between three rather than two or four slices. This complicates the message-passing implementation since, as illustrated in Fig. 7, in the assembly of the global system given by eq. (46) one needs to sum all the contributions (i.e. the internal forces computed separately in each slice) between slices. This problem is solved using a three-step sequence of messages: we first assemble the contributions between slices inside each chunk;
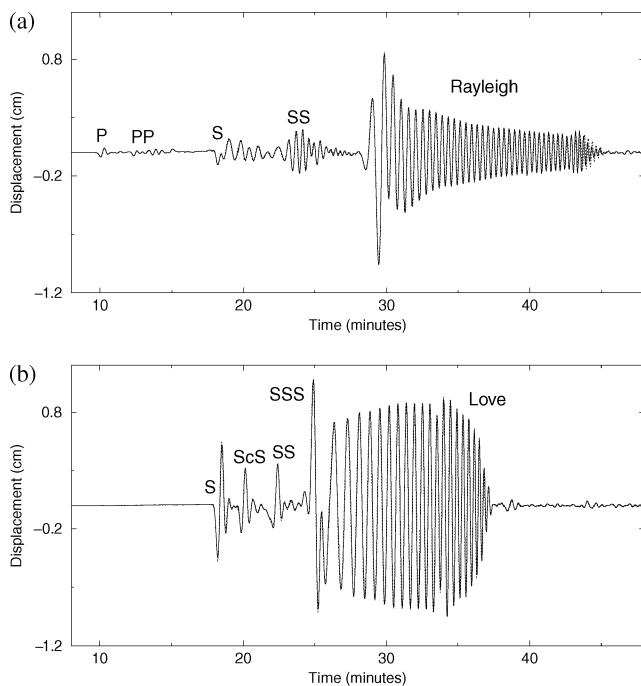
then between slices located on the edges of different chunks, excluding the corners of valence 3; then in a last step we assemble these corners separately.

The mesh shown in Fig. 6 contains a total of approximately 2.6 million spectral elements. In each spectral element we use a polynomial degree $N = 4$ for the expansion of the Lagrange interpolants at the Gauss–Lobatto–Legendre points (as in eqs 34 and 35 for instance), which means each spectral element contains $(N + 1)^3 = 125$ points, and the total global system of eq. (46), counting common points on the edges only once, contains 180 million points (corresponding to approximately 483 million degrees of freedom since we solve for the three components of displacement at each grid point, except in the fluid outer core, where we solve for the scalar potential). Polynomial degrees around 4 or 5 have proven to be optimal for wave propagation problems using the SEM, since they provide the best trade-off between accuracy and time-integration stability (Seriani & Priolo 1994). After division of the mesh into slices, each processor is responsible for 17,000 elements; with a polynomial degree $N = 4$, this corresponds to roughly 1.2 million grid points per processor. It is worth mentioning that, because of the mesh coarsening with depth, as shown in Fig. 6, most of the elements are located in the upper part of the model, where the wave speeds are slowest: 13 per cent of the elements are in the crust, 70 per cent in the mantle, 16 per cent in the outer core, and 1 per cent in the inner core (the small central cube in Fig. 10 excluded, since it is handled by a
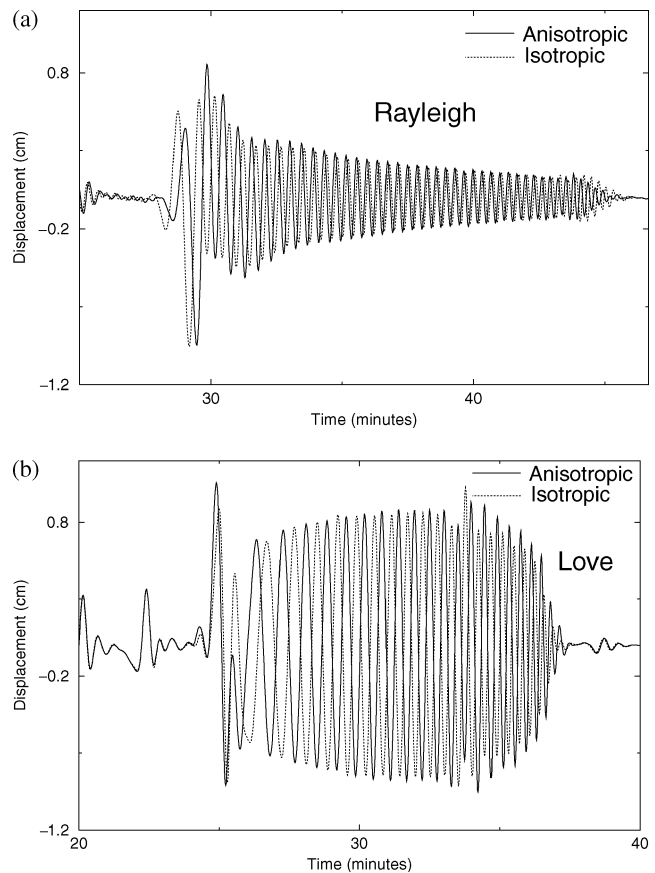
Figure 14. Comparison between normal-mode and SEM synthetics at an epicentral distance of $60°$ for the shallow Irian Jaya event. (a) Vertical component (b) Transverse component. Note the strongly dispersed surface waves and the excellent match for the body-wave arrivals.

Figure 15. Comparison between normal-mode synthetics for anisotropic PREM (solid line) and isotropic PREM (dotted line). The effect of an anisotropic asthenosphere is to significantly delay the Rayleigh wave, (a) vertical component, and slightly speed up the Love wave, (b) transverse component. Note that the SEM results shown in Fig. 14 capture the anisotropic effects very well.

separate processor). Therefore, most of the cost of the calculations comes from the upper mantle, and the entire core is almost negligible in terms of CPU time (also because in the outer core we solve for a scalar potential instead of a vector, which therefore further reduces the number of calculations).

The central cube in the inner core, shown in Fig. 10, poses yet another difficulty from a message-passing point of view. Since it is handled by a separate processor, and since it shares grid points with all the other slices, a separate communication pattern has been implemented based upon a master–slave programming philosophy: all the slices send their local contributions (the internal forces computed locally) to the central cube, which acts as a master, collecting and summing them, and then sending the result back to the slices, which act as slaves. The number of elements in the central cube is smaller than in any of the slices; this guarantees that the speed of the calculation is not governed by the processor responsible for the inner core (otherwise this would be a good example of poor load balancing).

5 RESULTS

In this section we carefully benchmark the SEM against normal-mode synthetics for anisotropic PREM without the ocean layer. We use the mesh and source-receiver geometry shown in Fig. 6. In each simulation the epicentre is located on the equator and the Greenwich meridian. Stations record ground displacement along the equator and the Greenwich meridian at 2 degree intervals. For reference, we used two normal-mode catalogues with a shortest period of 8 s: one without attenuation and another one with attenuation. No free-air, tilt, or gravitational potential corrections were applied (Dahlen & Tromp 1998).

The simulations presented in this section are accurate for periods greater than about 20 s. However, for routine, practical applications it is more convenient to use a step moment tensor in time and convolve with the desired moment-rate function $\dot{S}(t)$ later. This is perfec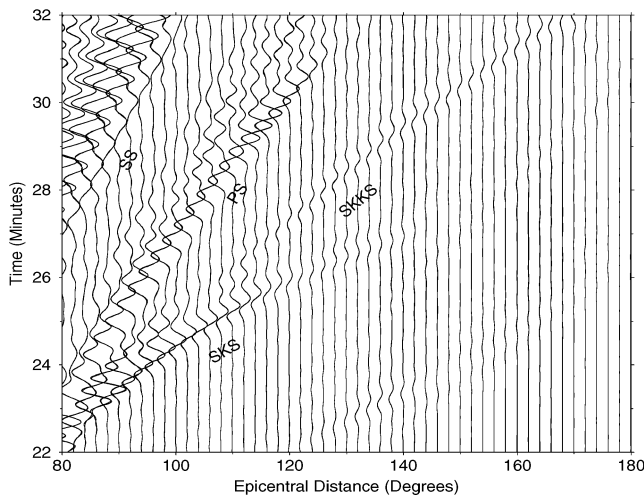tly acceptable in the SEM. In all the simulations we use a very short moment-rate function (an error function with a duration of one second). For the periods involved in the simulations this is equivalent to using a Heaviside function. We subsequently convolve the results with the desired moment-rate function (see Fig. 12 for the Gaussian source–time function used in the examples below). It is worth mentioning that the signals generated by this Heaviside-like source contain significant energy far above the resolution of both our grid (spatial resolution) and our time scheme (temporal resolution). This is not a problem since these artefacts remain in a frequency band that is later filtered by the convolution with the real source–time function. Comparisons, not shown here, between the convolved results and a SEM simulation based explicitly upon the source–time function in Fig. 12 showed that the two results are indistinguishable within the precision of the time scheme.

5.1 Shallow event

As a first example, we simulate the 1996 February 17 Irian Jaya earthquake. This large $M_w = 8.2$ event had its hypocentre at a depth of 15 km. Because of its shallow depth, the event generates strong surface waves, which provide a difficult test for the SEM: the free surface boundary condition, the thin, slow crust, and the anisotropic asthenosphere all come into play. The focal mechanism is shown in Fig. 11 and the moment-rate function in Fig. 12. The event has a half-duration of 18 s. Attenuation is turned off in this first simulation in order to validate the method for purely elastic, anisotropic media.

In Fig. 13 we show 90 min long vertical, radial and transverse record sections for epicentral distances from 0° to 360° and stations along the equator, as shown in Fig. 6. Each epicentral distance is associated with two traces: one calculated based upon normal-mode summation and the other based upon the SEM. The fact that the two synthetic seismograms are basically indistinguishable demonstrates that the SEM synthetics are very accurate. Many classical teleseismic body-wave arrivals can be easily distinguished. On the vertical and radial component one can clearly see P, S and their surface bounces, as well as the strongly dispersed Rayleigh wave. On the radial component one can discern the core reflected shear waves ScS_{1-4}, as well as SKS and $SKKS$. On the transverse component, S, SS, SSS, and $SSSS$ are very prominent, and so are ScS_{1-5}, and the Love wave. Note that near the antipode, where energy is arriving from all directions and the transverse component has little meaning,
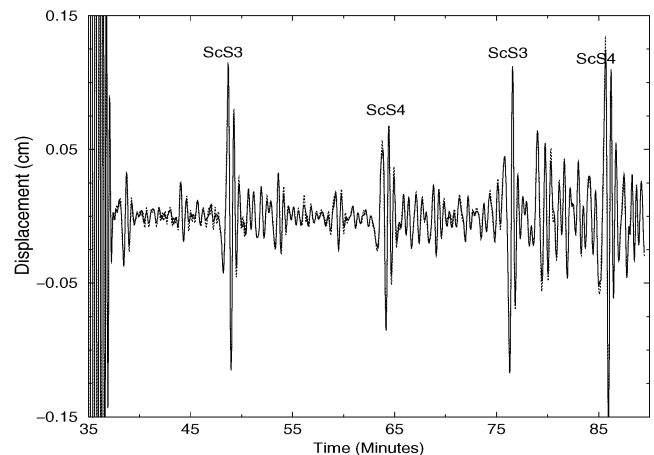

Figure 16. Record section comparison between SEM (solid lines) and mode (dotted lines) synthetics for core-sensitive body-wave arrivals SKS and SKKS between 80° and 180°. At each epicentral distance we plot both the SEM and the mode solutions, which are basically indistinguishable. The accurate predictions for SKS and SKKS validate the domain decomposition between the fluid and solid regions of the model as well as the potential used to represent the inhomogeneous fluid discussed in Section 3.2. Note that the converted phase PS is also very well modelled.

Figure 17. Comparison between SEM (solid line) and mode (dotted line) synthetics for *ScS* multiples on the transverse component. *ScS*$_3$ and *ScS*$_4$ are seen twice: once propagating along the minor arc and a second time propagating along the major arc. These core-reflected *SH* waves are roughly 20 times smaller in amplitude than the dominant Love wave (Fig. 14).

SKKS energy can be seen around 32 min in both the mode and the SEM solutions.

In Fig. 14 we show a more detailed comparison between normal-mode and SEM synthetics at an epicentral distance of 60°. Because the mode synthetics are only quasi-analytical, and therefore also contain some numerical errors, we do not show the difference between the SEM and normal-mode synthetics since this is not an objective estimate of the accuracy of the SEM. The figure
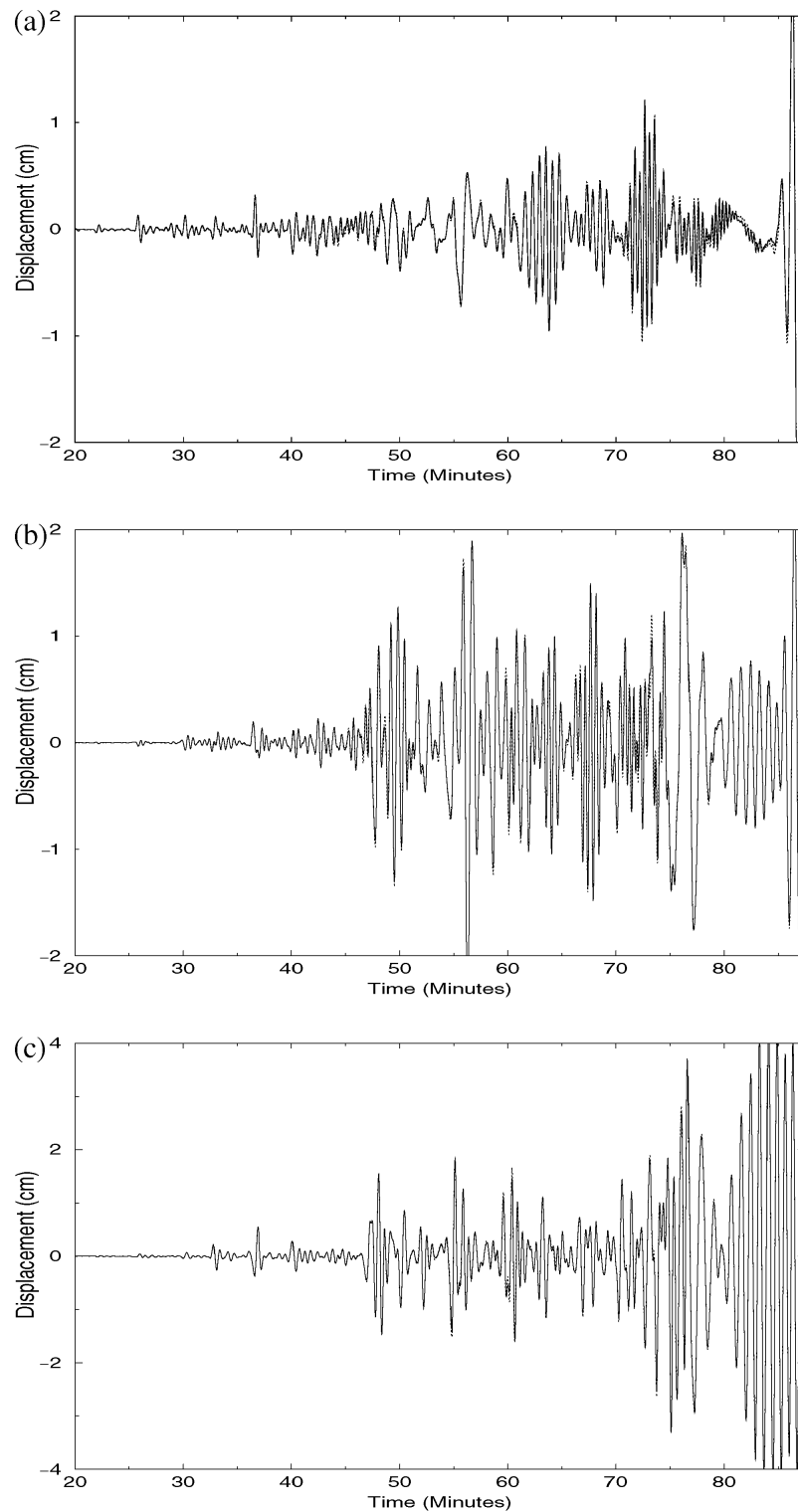

Figure 18. Comparison between SEM (solid line) and mode (dotted line) synthetics at the antipode. This is a difficult location because rays emanating from the source converge simultaneously from all directions, plus the epicentral distance is largest, leading to maximal numerical dispersion in a 90 min record. Again the mode and SEM synthetics on the (a) vertical, (b) radial and (c) transverse components are in excellent agreement. Note that in an elastic Earth model, focusing at the antipode is rather dramatic for surface waves: the amplitude of the Love wave exceeds 4 cm.

Table 1. Strain relaxation times used to reproduce the appropriate PREM Q values using three standard linear solids in parallel. The stress relaxation times used are the same for all five regions: $\tau_1^\sigma = 159.15494$ s, $\tau_2^\sigma = 22.50791$ s, and $\tau_3^\sigma = 3.18310$ s.

Depth range (km)	Q	τ_1^ϵ (s)	τ_2^ϵ (s)	τ_3^ϵ (s)
0–80	600	159.56831	22.55187	3.19149
80–220	80	162.01122	22.85290	3.24777
220–670	143	160.82505	22.69650	3.21878
670–2891 (CMB)	312	159.94162	22.59299	3.19930
5150 (ICB)–6371	84.6	161.87152	22.83321	3.24415

illustrates the level of accuracy for *P*, *PP*, *S*, and *SS* body waves as well as the Rayleigh wave on the vertical component. On the transverse component, body-wave arrivals *S*, *SS*, *SSS* and *ScS* can all be clearly discerned and are very well matched. As illustrated in Tromp & Komatitsch (2000), surface-wave dispersion is very sensitive to the detailed structure of the crust. The effects of the anisotropic asthenosphere are illustrated in Fig. 15 by comparing normal-mode synthetics for anisotropic and isotropic PREM. Anisotropy has a profound effect on the behaviour of surface waves. Note in particular that the Love wave is slightly faster in anisotropic
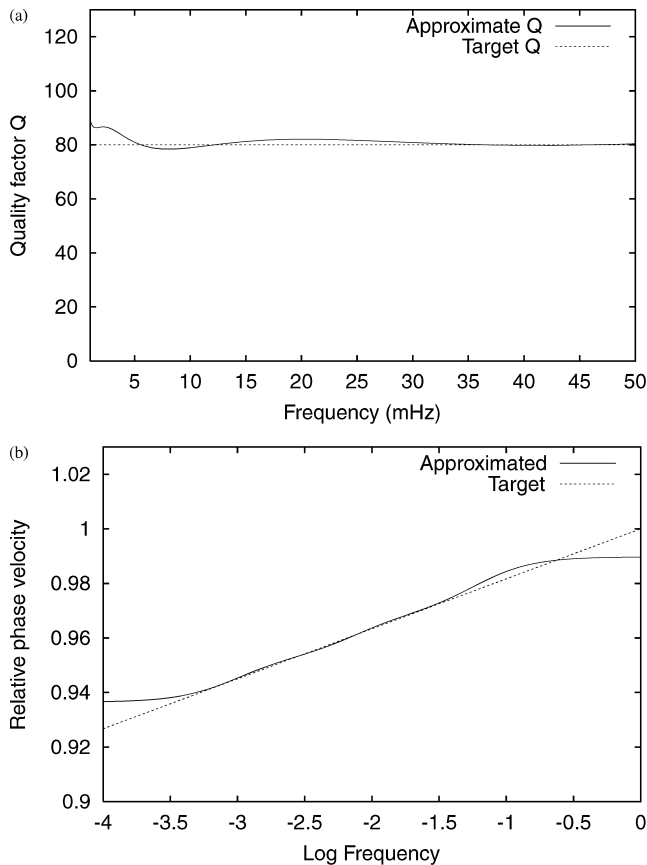
PREM, whereas the Rayleigh wave is significantly slower. These differences clearly illustrate the difficulties associated with the simulation of shallow events and demonstrate how well the SEM results in Figs 13 and 14 incorporate effects due to the crust and anisotropy.

The accuracy of the implementation of the inhomogeneous outer core based upon a scalar potential, as discussed in Section 3.2, is well illustrated by the *SKS* and *SKKS* arrivals in Fig. 16. The fact that normal modes and the SEM agree very well both in phase and in amplitude also validates the implementation of the domain decomposition between the fluid and solid regions of the model and the associated boundary conditions.

For *SH* waves the outer core acts as a free surface. Fig. 17 illustrates that core-reflected *SH* waves are accurately modelled up to *ScS*₄. These *ScS* multiples are about 20 times smaller in amplitude than the Love wave, which illustrates the level of accuracy in the synthetics (note the difference in vertical scale between Figs 14 and 17).

Probably the most difficult location for a comparison between normal modes and any numerical method is at the antipode, because of the convergence of all raypaths. In addition in our 90 min long simulation the antipode is also the point at which the waves have accumulated a maximum amount of numerical dispersion. Fig. 18 illustrates that the SEM results agree very well with the modes on all three components at this special location.
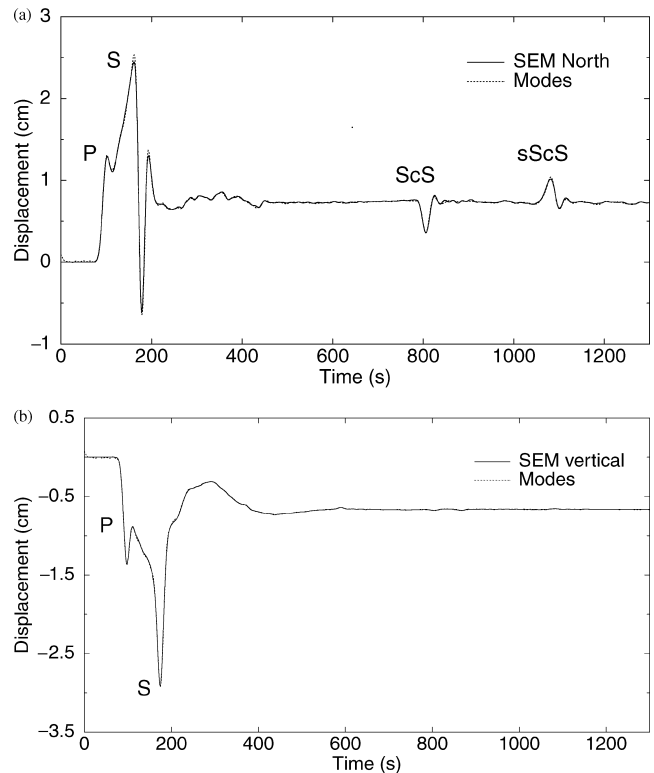

Figure 19. Approximation of an absorption-band model with a constant quality factor Q at periods between 20 and 1000 s based upon three standard linear solids. (a) Approximate quality factor (solid line) obtained by fitting a series of three linear solids to a constant Q of 80 (dotted line). Except at very long periods, the approximation is accurate to within a few per cent. (b) Physical dispersion associated with the absorption-band model. The physical dispersion associated with PREM is shown by the dotted line. Over the period range of interest, the series of three standard linear solids mimics the dispersion very well.

Figure 20. SEM (solid line) and mode (dotted line) synthetic seismograms for the great magnitude 8.2 1994 June 9 Bolivia earthquake recorded at station ST04 of the BANJO Array (e.g. Clarke *et al.* 1995). The depth of the event is 647 km. Anisotropy and attenuation are both included in this simulation. (a) North–south component, (b) vertical component. The east–west component is nodal for this station. Note the strong near field term linking the *P* and *S* wavefronts, the large 6.6 mm and 7.3 mm static offsets observed on the vertical and north–south components, respectively, as well as the strong *ScS* and *sScS* core-reflected phases.

5.2 Deep event

Our second simulation is for the 1994 June 9 deep Bolivia event of magnitude $M_w = 8.2$. The focal mechanism is illustrated in Fig. 11; the depth is 647 km. We use a moment-rate function similar to the one used for the Irian Jaya event (Fig. 12), but with a slightly shorter half-duration of 15 s.

At this point we wish to validate our implementation of attenuation in the method. Associated with PREM is a five-layer attenuation model. As mentioned earlier, we only incorporate shear attenuation: bulk attenuation can be safely neglected because the bulk Q is several hundred times larger than the shear Q. The calculation of normal-mode seismograms for anelastic Earth models is based upon first-order perturbation theory, which is acceptable for the attenuation associated with PREM (e.g. Dahlen & Tromp 1998); however as a consequence the mode synthetics in this section are not as accurate as in the purely elastic case of the previous section. For each layer we determine stress and stain relaxation times τ_ℓ^σ and τ_ℓ^ϵ for an absorption-band model over the period range between 20 and 1000 s, based upon three standard linear solids. Because of
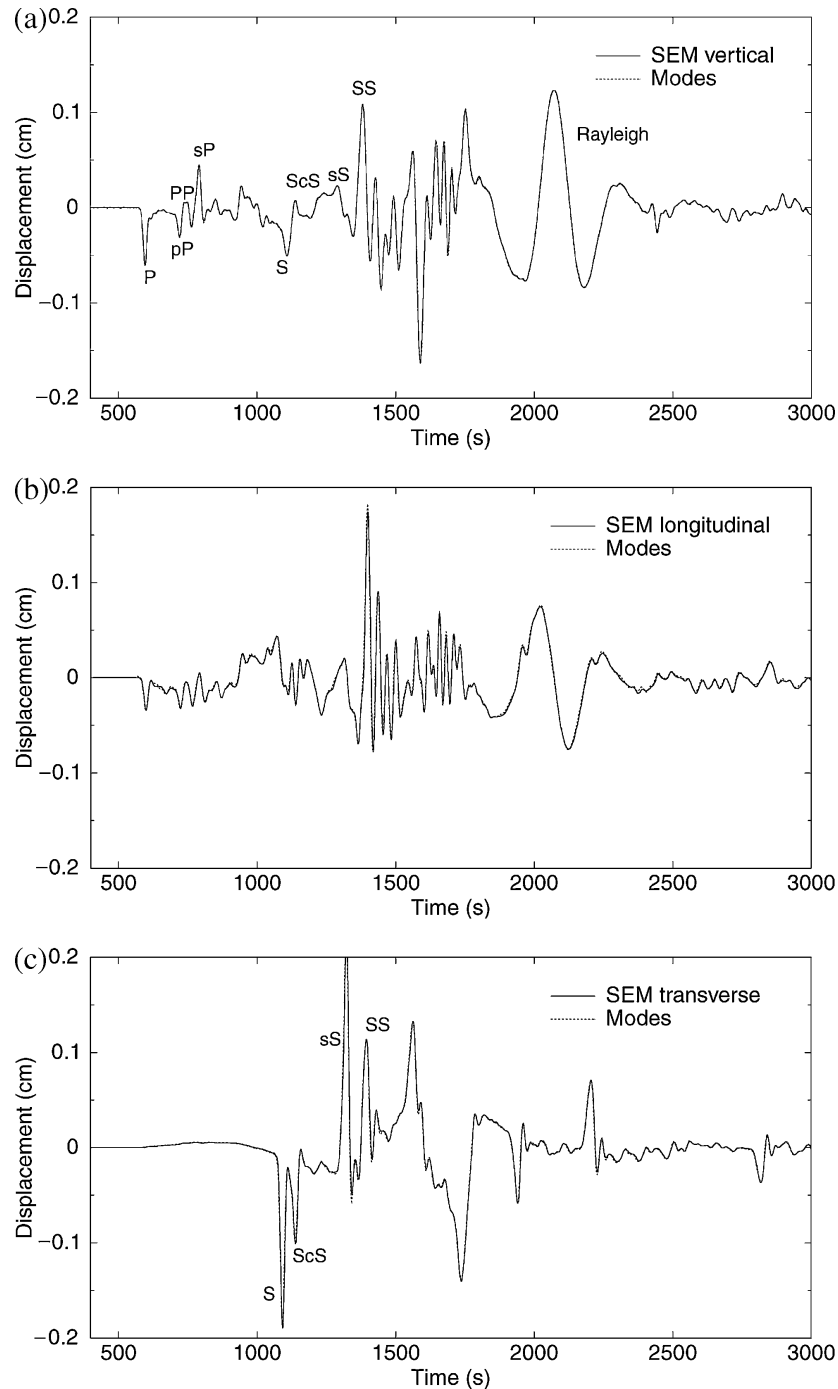
Figure 21. SEM (solid line) and mode (dotted line) synthetic seismograms for the great magnitude 8.2 1994 June 9 Bolivia earthquake, recorded at TriNet station PAS in Pasadena, California. The depth of the event is 647 km. Anisotropy and attenuation are both included in this simulation. (a) Vertical component, (b) longitudinal component, (c) transverse component. The agreement is almost perfect on the three components.

the broad period range, a solution based upon two solids does not give a satisfactory result. We evenly space the three stress relaxation times τ_ℓ^σ in logarithmic frequency. Next, we determine the strain relaxation times τ_ℓ^ϵ by minimizing the difference between the desired constant Q and predictions based upon the series of three standard linear solids using a simple iterative inversion scheme. Table 1 summarizes the stress and strain relaxation times used to reproduce the appropriate PREM Q values. Fig. 19 illustrates that the series of three standard linear solids can approximate a constant Q efficiently to within a few per cent. Associated with the absorption-band model is physical dispersion which affects the arrival times of the waves. To accommodate this, we take PREM, which has a reference frequency of 1 Hz, i.e. $\omega_0 = 2\pi$, and determine the shear modulus appropriate for a frequency ω_c at the logarithmic centre of the frequency range of interest (Liu *et al.* 1976):

$$\mu(\omega_c) = \mu(\omega_0)\left[1 + 2/(\pi Q_\mu)\ln(\omega_c/\omega_0)\right].\tag{49}$$

Given $\mu(\omega_c)$ we can calculate the relaxed modulus μ_R, from which we obtain the time dependent modulus $\mu(t)$ and the unrelaxed modulus μ_U based upon eqs (8) and (10), respectively. Fig. 19 also illustrates that, over the frequency band of interest, the dispersion associated with the PREM Q model is very well mimicked by three standard linear solids.

In Fig. 20 we compare normal-mode and SEM synthetics at station ST04 of the BANJO array in Bolivia at a distance of 5° south of the epicentre (more details about the BANJO array can be found in Clarke *et al.* 1995). This simulation is motivated by an experiment performed by Ekström (1995) who used normal-mode summation to analyze the static offset resulting from the event, and by the observations of a large offset in the BANJO data by Jiao *et al.* (1995). Again we find very good agreement between the modes and the SEM. In particular, the strong near-field term linking the *P* and *S* arrivals is accurately modelled, and the static offset of 6.6 mm on the vertical component and 7.3 mm on the North–South component is well recovered. Note also the distinct *ScS* arrival on this component at 800 s and the *sScS* arrival at 1080 s, which are perfectly reproduced. These *ScS* phases are clearly observed in the BANJO data (Clarke *et al.* 1995).

Next, we check the results of our simulation at teleseismic distance at the Pasadena, California, TriNet station PAS at an epicentral distance of 68°. Fig. 21 shows the three components of displacement both for the modes and the SEM. To appreciate the effects of attenuation and how accurately it has been modelled by the SEM, we show in Fig. 22 t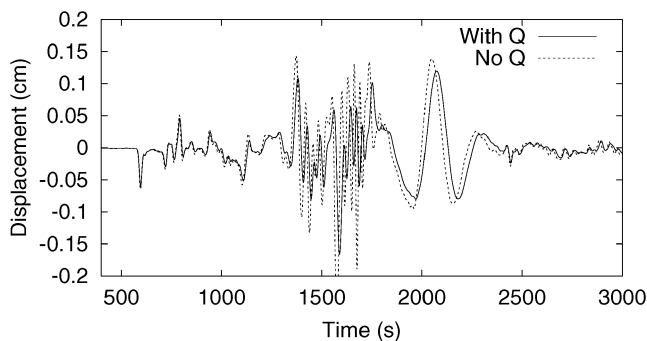he vertical component of displacement computed using modes with and without attenuation. One can see that the waveforms are significantly affected by attenuation, both in phase and amplitude. In Fig. 23 we compare our SEM synthetic seismogram for the vertical component of velocity at PAS to the real data. Both records have been lowpass-filtered with the same six-pole two-pass Butterworth filter with a corner period of 40 s, and our synthetics have been convolved with the instrument response. We note that this is the only time in this study that we filter our synthetics. The agreement is quite satisfactory, keeping in mind that our synthetics are based upon PREM and therefore do not include effects due to 3-D heterogeneity.

To illustrate that our implementation of the inner core is correct, we show in Fig. 24 a close-up of *PKP* arrivals on the vertical component. The *PKP* waveforms are very sensitive to the very high value of Poisson's ratio, 0.44, in the inner core: if the shear-wave velocity is not correctly represented, the *PKP* waveforms change considerably. Numerically this poses a challenge, because if the mesh is not fine enough the very slow inner-core shear-wave velocity of about 3.6 km s^{-1} is not sampled by enough points per wavelength. In our results, the *PKP*(AB) and *PKP*(BC) outer core branches as well as the *PKP*(DF) inner core branch are all very accurately modelled. A very weak P_{diff} arrival can be seen in the P shadow in both synthetics. The *PKP*(DF) arrival has travelled through the cube at the centre of the inner core, which is handled by one processor that needs to interact with all the other processors in the parallel implementation of the method, as explained previously. Note the very prominent depth phases, e.g. *pPKP*(DF), which arrive about two and a half minutes after the corresponding direct phases due to the large depth of the event. To appreciate the level of accuracy involved in the calculation of the *PKP* phases, note from Fig. 18 that the amplitudes of these arrivals are tiny compared to the later parts of the record (the depth of the event does not significantly affect this observation).

6 CONCLUSIONS

We have developed and implemented a spectral-element method (SEM) for the simulation of global seismic wave propagation. The method has been carefully benchmarked against normal-mode synthetics for elastic and anelastic versions of spherically symmetric earth model PREM. The SEM accurately incorporates effects due to the slow, thin crust, a transversely isotropic asthenosphere, sharp
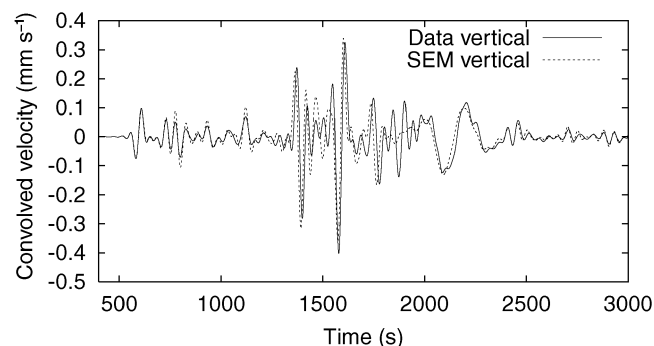
Figure 22. To illustrate the effects of attenuation and physical dispersion associated with anelastic PREM, we compare vertical component mode synthetics for PREM with (solid line) and without (dotted line) incorporating the effects of anelasticity. Note that elastic PREM is faster than anelastic PREM, and that in particular the S wave is significantly attenuated.

Figure 23. Comparison between SEM synthetics for anelastic, anisotropic PREM and real data recorded at TriNet station PAS in Pasadena, California, after the 1994 June 9 Bolivia event. Both vertical component velocity records have been lowpass-filtered with the same six-pole two-pass Butterworth filter with a corner period of 40 s, and the SEM synthetics have been convolved with the instrument response. This is the only time in this study that we filter SEM synthetics.
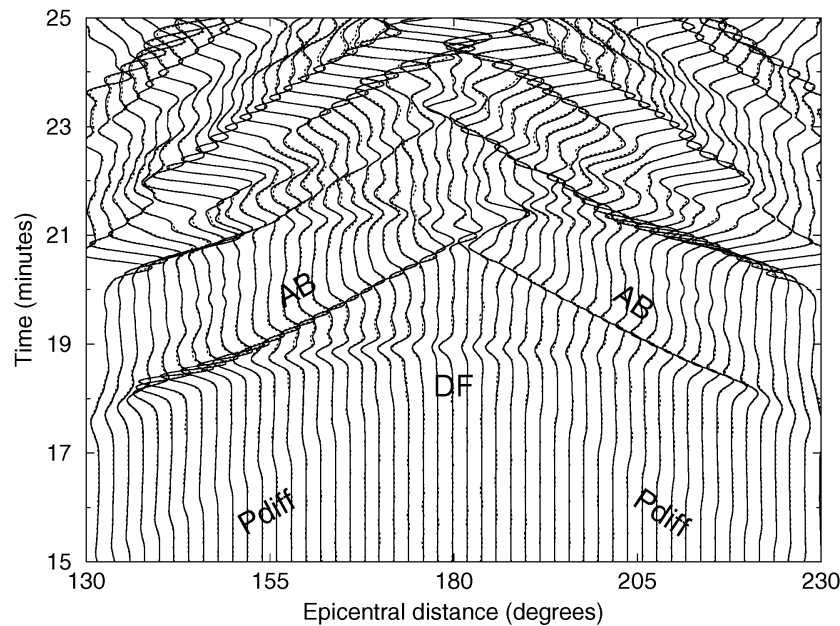
Figure 24. Record section comparison of *PKP* phases calculated for anelastic, anisotropic PREM based upon the SEM (solid lines) and modes (dotted lines) between 130° and 230° along the Greenwich meridian. At each epicentral distance we plot both the SEM and the mode solution. All *PKP* arrivals, including *PKIKP*, which has travelled through the central cube in the mesh, are well reproduced. Note also a very weak P_{diff} arrival in both synthetics between 130° and 170° and between 190° and 230°. This validates the master/slave parallel programming methodology that is used to implement the inner core, as illustrated in Fig. 10. It also demonstrates that we can correctly handle the unusually high value of Poisson's ratio in the inner core. Note from Fig. 18 that the size of the *PKP* arrivals around 20 min is tiny compared to later arrivals.

fluid–solid boundaries at the CMB and ICB, a high Poisson's ratio in the inner core and attenuation.

We emphasize that, for the same numerical cost, the SEM can accurately simulate wave propagation in fully 3-D Earth models that incorporate effects due to ellipticity and free surface topography with only a slight modification of the mesh used in this article. A crust with variable thickness and a laterally heterogeneous mantle can also be accommodated. The method currently does not incorporate effects due to the Earth's rotation, self-gravitation or the oceans. Rotation and self-gravitation only affect long-period surface waves, but the oceans are relevant for surface-reflected phases, such as *PP* or *SS*, and affect Rayleigh wave dispersion. These topics are the subject of another publication (Komatitsch & Tromp 2002).

The calculations presented in this article required 151 processors, 30 Gb of distributed memory for the elastic simulations, and 50 Gb of memory for the anelastic simulations (the anelastic memory requirements could be reduced considerably by spreading the memory variables used to model attenuation). They used tens of hours of CPU time, depending on the desired length of the seismograms. These requirements may seem formidable, but the fact of the matter is that the simulations can be performed on PC clusters that are comparable in price to less powerful shared-memory machines. Distributed computing on PC cluster computers using message passing has enabled individual investigators to perform numerical simulations that were previously barely possible on the most powerful supercomputers. Within ten years, computers reaching 1000 teraflops (1 petaflop) will be available (Sterling & Messina 1995), and the calculations presented in this study will be performed in a matter of seconds. This will open the door to tomographic inversions based upon SEMs.

REFERENCES

Bao, H., Bielak, J., Ghattas, O., Kallivokas, L.F., O'Hallaron, D.R., Shewchuk, J.R. & Xu, J., 1998. Large-scale simulation of elastic wave propagation in heterogeneous media on parallel computers, *Comput. Methods Appl. Mech. Eng.,* **152,** 85–102.

Bermúdez, A., Hervella-Nieto, L. & Rodriguez, R., 1999. Finite element computation of three-dimensional elastoacoustic vibrations, *J. Sound Vibr.,* **219,** 279–306.

Bernardi, C., Debit, N. & Maday, Y., 1990. Coupling finite element and spectral methods: first results, *Math. Comp.,* **54,** 21–39.

Bernardi, C., Maday, Y. & Patera, A.T., 1994. A new nonconforming approach to domain decomposition: the Mortar element method, in *Nonlinear Partial Differential Equations and Their Applications,* eds Brezis, H. & Lions, J.L., pp. 13–51, Séminaires du Collège de France, Pitman, Paris.

Canuto, C., Hussaini, M.Y., Quarteroni, A. & Zang, T.A., 1988. *Spectral Methods in Fluid Dynamics,* Springer-Verlag, New York.

Capdeville, Y., Stutzmann, E. & Montagner, J., 2000. Effect of a plume on long-period surface waves computed with normal-mode coupling, *Phys. Earth planet. Inter.,* **119,** 54–71.

Capdeville, Y., Chaljub, E., Vilotte, J.P. & Montagner, J.P., 2002. Coupling the spectral-element method with a modal solution for elastic wave propagation in global earth models, *Geophys. J. Int.,* in press.

Carcione, J.M., 1994. The wave equation in generalized coordinates, *Geophysics,* **59,** 1911–1919.

Carcione, J.M. & Wang, P.J., 1993. A Chebyshev collocation method for the wave equation in generalized coordinates, *Comp. Fluid Dyn. J.,* **2,** 269–290.

Carcione, J.M., Kosloff, D. & Kosloff, R., 1988. Wave propagation simulation in a linear viscoelastic medium, *Geophys. J. Int.,* **95,** 597–611.

Chaljub, E., 2000. Modélisation numérique de la propagation d'ondes sismiques en géométrie sphérique: application à la sismologie globale (Numerical modeling of the propagation of seismic waves in spherical geometry: application to global seismology), *PhD thesis,* Université Paris VII Denis Diderot, Paris, France.

Chaljub, E. & Tarantola, A., 1997. Sensitivity of SS precursors to topography on the upper-mantle 660-km discontinuity, *Geophys. Res. Lett.,* **24,** 2613–2616.

Chaljub, E., Capdeville, Y. & Vilotte, J.P., 2001. Solving elastodynamics in a fluid solid heterogeneous sphere: a parallel spectral element approximation on non-conforming grids, *J. Comput. Phys.,* submitted.

Clarke, T.J., Silver, P.G., Yeh, Y.L., James, D.E., Wallace, T.C. & Beck, S.L., 1995. Close in ScS and sScS reverberations from the 9 June 1994 Bolivian earthquake, *Geophys. Res. Lett.,* **22,** 2313–2316.

Cohen, G., Joly, P. & Tordjman, N., 1993. Construction and analysis of higher-order finite elements with mass lumping for the wave equation, in *Proceedings of the Second International Conference on Mathematical and Numerical Aspects of Wave Propagation,* pp. 152–160, ed. Kleinman, R., SIAM, Philadephia, PA.

Dahlen, F.A. & Tromp, J., 1998. *Theoretical Global Seismology,* Princeton University Press, Princeton.

Day, S.M., 1998. Efficient simulation of constant *Q* using coarse-grained memory variables, *Bull. seism. Soc. Am.,* **88,** 1051–1062.

Dziewonski, A.M. & Anderson, D.L., 1981. Preliminary reference Earth model, *Phys. Earth planet. Inter.,* **25,** 297–356.

Ekström, G., 1995. Calculation of static deformation following the Bolivia earthquake by summation of Earth's normal modes, *Geophys. Res. Lett.,* **22,** 2289–2292.

Emmerich, H. & Korn, M., 1987. Incorporation of attenuation into time-domain computations of seismic wave fields, *Geophysics,* **52,** 1252–1264.

Everstine, G.C., 1981. A symmetric potential formulation for fluid-structure interaction, *ASME J. Sound Vib.,* **79,** 157–160.

Faccioli, E., Maggio, F., Paolucci, R. & Quarteroni, A., 1997. 2D and 3D elastic wave propagation by a pseudo-spectral domain decomposition method, *J. Seismol.,* **1,** 237–251.

Felippa, C.A. & Deruntz, J.A., 1984. Finite-element analysis of shock-induced hull cavitation, *Comput. Methods Appl. Mech. Eng.,* **44,** 297–337.

Fischer, P.F. & Rønquist, E.M., 1994. Spectral-element methods for large scale parallel navier-stokes calculations, *Comput. Methods Appl. Mech. Eng.,* **116,** 69–76.

Furumura, T., Kennett, B.L.N. & Furumura, M., 1998. Seismic wavefield calculation for laterally heterogeneous whole earth models using the pseudospectral method, *Geophys. J. Int.,* **135,** 845–860.

Geller, R.J. & Ohminato, T., 1994. Computation of synthetic seismograms and their partial derivatives for heterogeneous media with arbitrary natural boundary conditions using the Direct Solution Method, *Geophys. J. Int.,* **116,** 421–446.

Gropp, W., Lusk, E. & Skjellum, A., 1994. *Using MPI, Portable Parallel Programming with the Message-Passing Interface,* MIT Press, Cambridge.

Gropp, W., Lusk, E., Doss, N. & Skjellum, A., 1996. A high–performance, portable implementation of the MPI message passing interface standard, *Parallel Computing,* **22,** 789–828.

Guo, B. & Babuška, I., 1986. The *h-p* version of the finite-element method, *Comput. Mech.,* **1,** 21–41.

Hara, T., Tsuboi, S. & Geller, R., 1991. Inversion for laterally heterogeneous earth structure using a laterally heterogeneous starting model: preliminary results, *Geophys. J. Int.,* **104,** 523–540.

Heaney, S., 2000. *Beowulf, A New Verse Translation, Bilingual Edition,* Farrar, Straus and Giroux Publishers, New York.

Hughes, T.J.R., 1987. *The Finite-Element Method, Linear Static and Dynamic Finite Element Analysis,* Prentice-Hall International, Englewood Cliffs, NJ.

Igel, H., 1999. Wave propagation in three-dimensional spherical sections by the Chebyshev spectral method, *Geophys. J. Int.,* **136,** 559–566.

Igel, H. & Geller, R., 2000. Numerical modeling of global seismic wave propagation: algorithms, accuracy, verification, *Phys. Earth planet. Inter.,* **119,** 1–2.

Igel, H. & Weber, M., 1996. P-SV wave propagation in the whole mantle using high-order finite differences: application to lowermost mantle structure, *Geophys. Res. Lett.,* **23,** 415–418.

Jiao, W., Wallace, T.C. & Beck, S.L., 1995. Evidence for static displacements from the June 9, 1994 deep Bolivian earthquake, *Geophys. Res. Lett.,* **22,** 2285–2288.

Kallivokas, L.F. & Bielak, J., 1993. Time-domain analysis of transient structural acoustics problems based on the finite-element method and a novel boundary element, *J. acoust. Soc. Am.,* **94,** 3480–3492.

Komatitsch, D., 1997. Méthodes spectrales et éléments spectraux pour l'équation de l'élastodynamique 2D et 3D en milieu hétérogène (Spectral and spectral-element methods for the 2D and 3D elastodynamics equations in heterogeneous media), *PhD thesis,* Institut de Physique du Globe, Paris, France.

Komatitsch, D. & Tromp, J., 1999. Introduction to the spectral-element method for 3-D seismic wave propagation, *Geophys. J. Int.,* **139,** 806–822.

Komatitsch, D. & Tromp, J., 2002. Spectral-element simulations of global seismic wave propagation-II. 3-D models, oceans, rotation, and self-gravitation, *Geophys. J. Int.,* in press.

Komatitsch, D. & Vilotte, J.P., 1998. The spectral-element method: an efficient tool to simulate the seismic response of 2D and 3D geological structures, *Bull. seism. Soc. Am.,* **88,** 368–392.

Komatitsch, D., Barnes, C. & Tromp, J., 2000a. Wave propagation near a fluid-solid interface: a spectral element approach, *Geophysics,* **65,** 623–631.

Komatitsch, D., Barnes, C. & Tromp, J., 2000b. Simulation of anisotropic wave propagation based upon a spectral-element method, *Geophysics,* **65,** 1251–1260.

Lahaye, D.J.P., Maggio, F. & Quarteroni, A., 1997. Hybrid finite element-spectral element approximation of wave propagation problems, *East-West J. Numer. Math.,* **5,** 265–289.

Lesieur, M., 1997. *Turbulence in Fluids,* Kluwer Academic Publishers, Dordrecht.

Liu, H.P., Anderson, D.L. & Kanamori, H., 1976. Velocity dispersion due to anelasticity: implications for seismology and mantle composition, *Geophys. J. R. astr. Soc.,* **47,** 41–58.

Lognonné, P. & Romanowicz, B., 1990. Modeling of coupled normal modes of the Earth: the spectral method, *Geophys. J. Int.,* **102,** 365–395.

Love, A.E.H., 1911. *Some Problems of Geodynamics,* Cambridge University Press, Cambridge.

Maday, Y. & Patera, A.T., 1989. Spectral element methods for the incompressible Navier-Stokes equations, in *State of the Art Survey in Computational Mechanics,* pp. 71–143, eds Noor, A.K. & Oden, J.T.

Moczo, P., Bystrický, E., Kristek, J., Carcione, J.M. & Bouchon, M., 1997. Hybrid modeling of *P-SV* seismic motion at inhomogeneous viscoelastic topographic structures, *Bull. seism. Soc. Am.,* **87,** 1305–1323.

Pacheco, P.S., 1997. *Parallel Programming with MPI,* Morgan Kaufmann Press, San Francisco.

Paolucci, R., Faccioli, E. & Maggio, F., 1999. 3D response analysis of an instrumented hill at Matsuzaki, Japan, by a spectral method, *J. Seismol.,* **3,** 191–209.

Park, J., 1986. Synthetic seismograms from coupled free oscillations: the effects of lateral structure and rotation, *J. geophys. Res.,* **91,** 6441–6464.

Park, J. & Yu, Y., 1992. Anisotropy and coupled free oscillations: simplified models and surface wave observations, *Geophys. J. Int.,* **110,** 401–420.

Park, K.C. & Felippa, C.A., 1980. Partitioned transient analysis procedures for coupled field problems: accuracy analysis, *J. Appl. Mech.,* **47,** 916–926.

Patera, A.T., 1984. A spectral-element method for fluid dynamics: laminar flow in a channel expansion, *J. Comput. Phys.,* **54,** 468–488.

Priolo, E., Carcione, J.M. & Seriani, G., 1994. Numerical simulation of interface waves by high-order spectral modeling techniques, *J. acoust. Soc. Am.,* **95,** 681–693.

Robertsson, J.O.A., 1996. A numerical free-surface condition for elastic/viscoelastic finite-difference modeling in the presence of topography, *Geophysics,* **61,** 1921–1934.

Ronchi, C., Ianoco, R. & Paolucci, P.S., 1996. The 'Cubed Sphere': a new method for the solution of partial differential equations in spherical geometry, *J. Comput. Phys.,* **124,** 93–114.

Sadourny, R., 1972. Conservative finite-difference approximations of the primitive equations on quasi-uniform spherical grids, *Monthly Weather Rev.,* **100,** 136–144.

Seriani, G., 1998. 3-D large-scale wave propagation modeling by a spectral-element method on a Cray T3E multiprocessor, *Comput. Methods Appl. Mech. Eng.,* **164,** 235–247.

Seriani, G. & Priolo, E., 1994. A spectral-element method for acoustic wave simulation in heterogeneous media, *Finite Elements in Analysis and Design,* **16,** 337–348.

Seriani, G., Priolo, E. & Pregarz, A., 1995. Modelling waves in anisotropic media by a spectral-element method, in *Proceedings of the Third International Conference on Mathematical and Numerical Aspects of Wave Propagation,* pp. 289–298, ed. Cohen, G., SIAM, Philadephia, PA.

Sterling, T.L. & Messina, P.C., 1995. *Enabling Technologies for Petaflops Computing,* MIT Press, Cambridge.

Sterling, T.L., Salmon, J., Becker, D.J. & Savarese, D.F., 1999. *How to Build a Beowulf, a Guide to the Implementation and Application of PC Clusters,* MIT Press, Cambridge.

Takeuchi, N., Geller, R. & Cummins, P., 2000. Complete synthetic seismograms for 3-D heterogeneous Earth models computed using modified DSM operators and their applicability to inversion for Earth structure, *Phys. Earth planet. Inter.,* **119,** 25–36.

Tarnow, N. & Simo, J.C., 1994. How to render second-order accurate time-stepping algorithms fourth-order accurate while retaining the stability and conservation properties, *Comput. Methods Appl. Mech. Engrg.,* **115,** 233–252.

Taubes, G., 1996. Do-it-yourself supercomputers, *Science,* **274,** 1840.

Taylor, M., Tribbia, J. & Iskandarani, M., 1997. The spectral-element method for the shallow water equation on the sphere, *J. Comput. Phys.,* **130,** 92–108.

Tessmer, E., Kessler, D., Kosloff, D. & Behle, A., 1992. Multi-domain Chebyshev-Fourier method for the solution of the equations of motion of dynamic elasticity, *J. Comput. Phys.,* **100,** 355–363.

Thomas, C., Igel, H., Weber, M. & Scherbaum, F., 2000. Acoustic simulation of *P*-wave propagation in a heterogeneous spherical earth: numerical method and application to precursor waves to *PKPdf, Geophys. J. Int.,* **141,** 6441–6464.

Thompson, L.L. & Pinsky, P., 1996. A space-time finite-element method for structural acoustics in infinite domains. Part 1: formulation, stability and convergence, *Comput. Methods Appl. Mech. Eng.,* **132,** 195–227.

Tromp, J. & Komatitsch, D., 2000. Spectral-element simulations of wave propagation in a laterally homogeneous Earth model, in *Problems in Geophysics for the New Millenium,* pp. 351–372, eds Boschi, E., Ekström, G. & Morelli, A., INGV, Roma, Italy.

Zeng, X., 1996. Finite difference modeling of viscoelastic wave propagation in a generally heterogeneous medium in the time domain, and a dissection method in the frequency domain, *PhD thesis,* University of Toronto, Canada.

Zienkiewicz, O.C., 1977. *The Finite Element Method in Engineering Science,* 3rd edn, McGraw-Hill, New York.